FilamentID reveals the composition and function of metabolic enzyme polymers during gametogenesis

Authors

Jannik Hugener†[1,2,3], Jingwei Xu†[1], Rahel Wettstein[2,3], Lydia Ioannidi[3], Daniel Velikov[3,4], Florian Wollweber[1], Adrian Henggeler[2,3], Joao Matos[2,3*] and Martin Pilhofer[1*]

Affiliations

[1]Institute of Molecular Biology and Biophysics, ETH Zürich, 8093 Zürich, Switzerland.

[2]Institute of Biochemistry, ETH Zürich, 8093 Zürich, Switzerland.

[3]Max Perutz Labs, University of Vienna, 1030 Vienna, Austria.

[4]Vienna BioCenter PhD Program, Doctoral School of the University of Vienna and Medical University of Vienna, 1030 Vienna, Austria.

† both authors contributed equally to this work

*corresponding authors: joao.matos@univie.ac.at and pilhofer@biol.ethz.ch

SUMMARY

Gamete formation and subsequent offspring development often involve extended phases of suspended cellular development or even dormancy. How cells adapt to recover and resume growth remains poorly understood. Here, we visualized budding yeast cells undergoing meiosis by cryo-electron tomography (cryoET) and discovered elaborate filamentous assemblies decorating the nucleus, cytoplasm, and mitochondria. To determine filament composition, we developed a "Filament IDentification" (FilamentID) workflow that combines multiscale cryoET/cryo-electron microscopy (cryoEM) analyses of gently lysed cells. FilamentID identified the mitochondrial filaments as the conserved aldehyde dehydrogenase Ald4^{ALDH2} and the nucleoplasmic/cytoplasmic filaments being composed of acetyl-CoA synthetase Acs1^{ACSS2}. The near-native high-resolution structures revealed the mechanism underlying polymerization and enabled us to perturb filament formation. Acs1 polymerization facilitates the recovery of chronologically aged spores, and more generally, the cell cycle re-entry of starved cells. FilamentID is broadly applicable to characterize filaments of unknown identity in diverse cellular contexts.

16 **HIGHLIGHTS**

17 • FilamentID: a multiscale imaging workflow to characterize cellular filaments of unknown
18   composition

19 • The conserved aldehyde dehydrogenase Ald4[ALDH2] polymerizes into filament arrays within meiotic
20   mitochondria

21 • The conserved acetyl-CoA synthetase Acs1[ACSS2] forms filament arrays in the nucleus and the
22   cytoplasm

23 • Metabolites mediate Acs1 polymerization to store Acs1 in an inactive state in gametes and starved
24   cells

25 • Acs1 filament formation is required for efficient return to growth from starvation stress

26

INTRODUCTION

Most organisms live in rapidly changing environments and frequently experience adverse conditions for growth and reproduction. In microorganisms, one common response to environmental stress is the reversible entry into a dormant state, in which cells reduce their metabolic activity and arrest proliferation. Dormancy can also involve the execution of specialized developmental programs that result in differentiated cell types, such as spores, which can withstand nutrient scarcity, non-optimal temperatures, or desiccation. The formation of dormant cells typically relies on extensive remodeling of the cellular architecture, including, amongst others, changes in cell size, cell envelope structure, or cytoplasmic density and composition [1,2]. These ultrastructural adaptations are thought to enable cells to enter, maintain, and recover from dormancy, but their underlying molecular mechanisms remain poorly understood.

A hallmark feature of cellular dormancy is a decrease in metabolic activity [1]. In addition to the downregulation of enzyme function through the modulation of gene expression, an emerging concept posits that metabolic activity can be spatiotemporally controlled by enzyme self-assembly into filamentous polymers or agglomerates. Subcellular compartmentalization of metabolic enzymes mediated by self-association has been observed in different domains of life and has often been associated with cellular starvation [3-9]. In the budding yeast *Saccharomyces cerevisiae*, genome-wide fluorescence light microscopy screens have revealed a surprisingly high number of enzymes that form punctate or rod-shaped structures in response to the metabolic state of the cell [10-13]. Notable examples include the cytidine triphosphate synthase CTP [14,15], the glutamine synthetase Gln1 [16], the translation initiation factor elF2B [17], or the glucokinase Glk1 [18]. In all four cases, filament formation has been proposed to play important roles in the regulation of enzyme activity and, as such, to be of relevance for cell physiology. Even though biochemical reconstitution approaches coupled with structural studies have begun to shed light on the mechanistic basis of filament organization, it remains challenging to ascertain filament structural organization in the cellular context. Moreover, whether filament formation occurs and plays specialized roles in other biological contexts, for example when cells enter prolonged periods of developmental arrest or dormancy after gametogenesis, remains to be determined.

In many sexually reproducing organisms, including budding yeast, cells enter gametogenesis as a natural response to nutrient deprivation, resulting in the production of highly differentiated spores [19]. The principal features of meiosis are evolutionarily conserved and include a single round of DNA replication, followed by two consecutive nuclear divisions, termed meiosis I and meiosis II [20]. At the completion of meiosis, a haploid DNA complement, cytoplasmic content, and organelles are inherited by four arising gametes, which are protected by a thick spore wall. The resistant spores remain viable in a dormant state, preserving the potential to resume growth after encountering favorable environments [19]. How spores

61   preserve all essential cellular components required for the resumption of growth over potentially very

62   long periods of time remains unclear.

63   Here, we have used cryo-electron tomography (cryoET) imaging to study budding yeast cells throughout

64   gametogenesis, since it allows the visualization of mesoscale assemblies in their cellular context in a

65   near-native state [21,22]. We discovered distinct types of previously uncharacterized filament assemblies in

66   different cellular compartments. Since the identification of such structures by cryoET remains

67   exceptionally challenging, we developed a workflow to image gently lysed cells by employing a

68   combination of cryoET and single-particle cryo-electron microscopy (cryoEM), which we have termed

69   FilamentID. By enabling us to obtain high-resolution structures in near-native conditions, FilamentID

70   allowed the unambiguous identification of two distinct types of polymerized metabolic enzymes.

71   Targeted mutations and downstream functional experiments suggest that metabolic enzyme

72   polymerization is induced during starvation and required for efficient gamete awakening after prolonged

73   dormancy.

74

75 **RESULTS**

76 **Filament assemblies form in mitochondria, nucleus, and cytoplasm of yeast cells undergoing**
77 **gametogenesis**

78 We set out to visualize ultrastructural adaptations of cells undergoing gametogenesis upon nutrient
79 starvation. To this end, we synchronized diploid *S. cerevisiae* cells at G0/G1 through gradual starvation
80 and induced meiosis by transferring the cultures into sporulation medium (SPM) lacking a nitrogen
81 source, as previously described (Figure S1A) [23,24]. Fluorescence activated cell sorting (FACS analysis)
82 of DNA content showed that most cells were in G0/G1 prior to transfer to SPM and efficiently underwent
83 DNA replication between two and four hours after induction of meiosis (Figure S1B). For imaging in a
84 near-native state, meiotic cells were plunge-frozen on EM grids, thinned by cryo-focused ion beam
85 (cryoFIB) milling, and imaged by cryoET [25]. To reduce cell-to-cell variability that could arise from
86 asynchronous meiotic progression, in an initial step we used prophase I-arrested cultures (*ndt80Δ*) [26]
87 that were collected eight hours after induction of meiosis.

88 We observed various filamentous assemblies in different sub-cellular compartments (Figure 1A-C). One
89 type of filament was frequently observed in mitochondria, hereafter referred to as "mitochondrial
90 filament." In longitudinal views, these filaments appeared straight and were often bundled together.
91 Cross-sections in the representative cryo-tomogram revealed that the filament bundles were ordered in
92 arrays of ~40 individual filaments. A second type of filament was found in the nucleus and in the
93 cytoplasm, hereafter referred to as "nucleocytoplasmic" filament. These nucleocytoplasmic filaments
94 were also arranged in filament bundles, however, the organization appeared more heterogeneous and
95 complex, with some filaments branching away from the bundles. Cross-sections of individual
96 nucleocytoplasmic filaments showed a triangular architecture.

97 Quantification of the two filament types revealed that mitochondrial filaments were present in ~28% of
98 the imaged mitochondria (n = 23/81), and nucleocytoplasmic filaments in ~7% of the tomograms
99 containing nuclear volume (n = 2/29) and ~4% of the tomograms containing cytoplasmic volume (n =
100 3/76) (Figure 1D). Importantly, no filaments were observed in mitotically dividing cells grown in rich
101 medium, indicating that meiosis, or the process of starvation-induced gametogenesis, may drive the
102 formation of such structures.

103 **FilamentID: a workflow to identify cellular filaments of unknown molecular composition**

104 Conventional approaches to identify filaments seen *in cellulo* would be either A) the generation of high-
105 resolution sub-tomogram averages, or B) the purification of the filaments followed by downstream
106 single-particle cryoEM analyses. For the identification of filaments, both approaches are very
107 challenging, since the abundance of the filaments is relatively low and their identities are unknown. We

108   therefore developed a "Filament IDentification" (FilamentID) workflow that is applicable to low-
109   abundance targets (problematic for approach "A") and that circumvents the need for purification of the
110   complex of interest (required for approach "B"). One critical aspect of the workflow entails the
111   preparation of the sample such that it can be imaged without the need for cryo-sample thinning. Towards
112   this goal, we adapted a chromosome surface spreading protocol [27,28] to gently lyse and "spread" either
113   isolated organelles or entire cells onto EM grids. Since cell envelope and organelle integrity become
114   partially disrupted, the cellular contents are diluted, making intracellular complexes directly accessible
115   for a combination of cryoET and single-particle cryoEM imaging.

116   The workflow features two variations for the identification of filaments in mitochondria or
117   nucleoplasm/cytoplasm, respectively (Figure 2). Step 1: Cells are spheroplasted by digesting the cell
118   wall with Zymolyase. For the identification of mitochondrial filaments, mitochondria are then purified
119   and spread onto EM grids by hypo-osmotic swelling. For the identification of nucleocytoplasmic
120   filaments, entire spheroplasts are spread onto an EM grid by hypo-osmotic swelling and the addition of
121   a mild detergent. Step 2: Grids are vitrified by plunge-freezing. Step 3: Samples are subjected to data
122   collection. Each sample is imaged by recording tilt-series for cryoET, as well as 2D projection images
123   for targeted single-particle cryoEM. Step 4: CryoET data is used to generate low-resolution sub-
124   tomogram averages to assess filament symmetry. The single-particle data are used to generate high-
125   resolution maps by helical reconstruction, based on the symmetry information determined by cryoET.
126   Step 5: Integrating the cryoEM data with structure prediction, structure databases, and proteomic
127   analyses allows for the unambiguous identification of the filament components. Step 6: Structural
128   findings are validated by genetically interfering with filament polymerization. The resulting point
129   mutants can be used in functional assays to reveal the role of filament formation. We note that the
130   imaging of entire spread spheroplasts would also be fully compatible with the identification of
131   mitochondrial filaments. However, the mitochondrial purification step is useful in order to reduce the
132   workload in steps 3-5.

133   **The conserved mitochondrial aldehyde dehydrogenase Ald4 polymerizes into filaments**

134   We first applied FilamentID to characterize the mitochondrial filaments. To determine whether we could
135   preserve the filament arrays after organelle purification, we imaged isolated mitochondria by cryoET.
136   We observed the characteristic mitochondrial double membrane, cristae decorated with F_OF_1-ATP
137   synthase, as well as individual filaments and ordered filament arrays (Figure 3A and S2). Sub-tomogram
138   averaging of the filaments revealed a repetitive two-fold symmetric architecture that matches the *in*
139   *cellulo* observations (Figure 1A-C and 3B).

140   Next, we collected single-particle cryoEM data of spread mitochondria. Due to the heterogeneous
141   distribution of the filaments on the grid, we employed a targeted single-particle cryoEM data collection
142   strategy, where we extensively screened grid squares at low magnification, followed by high-

6

143   magnification data collection (Figure 3C). As detailed below, due to the repetitive architecture of the

144   filaments, a small dataset of several hundred micrographs was sufficient for filament identification. For

145   helical reconstruction, we used the symmetry information obtained from sub-tomogram averaging as a

146   starting point to interpret the helical parameters of the filament in real space (Figure 2). We determined

147   an initial filamentous structure at 6.8 Å resolution (Figure S3A). As the resolution was not sufficient to

148   trace the Cα-backbone, we employed structural dockings of AlphaFold-predicted mitochondrial proteins

149   [29,30]. To identify potential candidates, we have used mass spectrometry (MS) analysis in a parallel study

150   to characterize the meiotic proteome [31], which revealed that various mitochondrial matrix/inner

151   membrane components [32] are upregulated at the onset gametogenesis (Figure S4A). Out of 30 candidate

152   proteins, we identified the metabolic enzyme aldehyde dehydrogenase 4 (Ald4) as the most likely

153   filament component (Figure S4B). Based on the knowledge that aldehyde dehydrogenases form

154   tetramers [33], we further performed 2D classification and found that the repeating subunits polymerize in

155   two distinct modes, helical and non-helical (Figure S3B). Therefore, we then treated the central part of

156   the helical segments as individual particles and determined the Ald4 tetramer at a final resolution of 3.8

157   Å (Figure S3C-D). Ald4 tetramers can stack together to form a helical filament architecture (rise = 83

158   Å, twist = ~180˚), which fitted our map from sub-tomogram averaging (Figure S4C). Moreover, Ald4

159   tetramers could also assemble in a head-to-head and tail-to-tail fashion (non-helical mode) (Figure 3D

160   and S3B-C).

161   To validate the presence of Ald4 in the filaments, we first analyzed the reconstructed map and found

162   that it was incompatible with other Ald isoforms present in yeast (Figure S3E, S4D & Table S1). In

163   addition, we generated an *ALD4* deletion mutant (*ald4Δ*), isolated mitochondria from meiotic cells, and

164   imaged them using cryoET. In *ald4Δ* strains, we did not observe any filaments in mitochondria (n =

165   0/77), whereas ~14% of the mitochondria from wild-type cells contained filaments (n = 10/71) (Figure

166   S4E).

167   To understand how Ald4 assembles into filaments, we exploited the tetramer stacking interfaces and

168   identified eight residues that potentially mediate filament polymerization (Figure 3E). We mutated these

169   eight residues and tested if strains expressing the interface mutations (*ald4^int^*) could form filaments in

170   isolated mitochondria. Notably, we did not detect any filaments in the *ald4^int^* mitochondria (n = 0/28),

171   whereas ~15% of the mitochondria from the *ALD4^WT^* control strain contained filaments (n = 5/33)

172   (Figure 3F). Western blotting showed that the expression levels of GFP-tagged *ALD4^WT^* and the *ald4^int^*

173   mutant were comparable (Figure 3G), suggesting that the interface mutations prevent filament assembly

174   without affecting the general stability of the protein.

175   In summary, our workflow unambiguously identified the mitochondrial filament arrays as

176   homopolymers of Ald4, and we report the first high-resolution structure of a eukaryotic polymerized

177   aldehyde dehydrogenase enzyme. Our filament identification is consistent with a previous report of

178   elongated inclusion bodies observed by conventional EM, which co-localized with Ald4 antibodies in

179 immuno-gold staining [34]. An accompanying paper [31] presents a characterization of the role of Ald4

180 polymerization during yeast gametogenesis.

The conserved acetyl-CoA synthetase Acs1 forms filament assemblies in the nucleus and the cytoplasm

183 We then applied FilamentID to characterize the nucleocytoplasmic filament assemblies (Figure 1 A-C).

184 To this end, we spread entire meiotic yeast cells directly on EM grids and plunge-froze them (Figure 2).

185 Spread spheroplasts appeared as disc-shaped densities, with ~4 μm diameter in low magnification

186 images (Figure S5A). Cryo-tomograms of spreads revealed not only a variety of different filament types,

187 but also other well-preserved molecular superstructures, such as spindle pole bodies connected via

188 microtubules (Figure S5A-B). Interestingly, the nucleocytoplasmic filaments were seen both as

189 individual filaments and organized as complex bundles (Figure 4A). In some of the tomograms we also

190 observed potential (dis-) assembly intermediates, where small filaments appear to converge into a large

191 filament bundle (Figure S5C). Sub-tomogram averaging of individual filaments revealed a triple-helical

192 complex with 5.5 nm ladder-like repeats (Figure 4B). The triangular shape of the averaged volume, as

193 well as the overall bundle organization resembled our initial observations *in cellulo* (Figure 1A-C).

194 To complement the cryoET data, we applied targeted single-particle cryoEM data collection (Figure

195 4C), followed by helical reconstruction (Figure S6A-B). This allowed us to obtain a filament structure

196 at ~3.5 Å resolution (Figure S6C-D), which was sufficient to directly trace the Cα-backbone of one

197 subunit. The backbone model was manually built and was then subjected to the Dali server [35], which

198 revealed the metabolic enzyme acetyl-coenzyme A synthetase 1 (Acs1) as a strong candidate.

199 To validate that the filament consists of Acs1 and not Acs2, a second isoform present in yeast, we

200 compared their sequences and analyzed densities of characteristic residues in our atomic model (Figure

201 S6E, Figure S7A & Table S1). In addition, we generated an *ACS1* deletion mutant (*acs1Δ*) and

202 performed cryoET on the spread spheroplasts of meiotic cells. We did not observe any

203 nucleocytoplasmic filament bundles in spreads from *acs1Δ* spheroplasts (n = 0/80), while ~32% of the

204 wild-type spheroplasts contained filament bundles (n = 20/63) (Figure S7B).

205 The filament architecture consists of layers of Acs1 trimers, which are related to consecutive layers

206 through a helical operation (rise = 53.61 Å, twist = 13.03˚), resulting in a filament with 13 nm diameter

207 (Figure 4D). Structural docking showed that Acs1 filaments had the same arrangements as seen in the

208 sub-tomogram average (Figure S7C), whereas the filament arrangement is different from the packing of

209 yeast Acs1 in the previously resolved crystal structure (PDB entry: 1RY2) (Figure S7D) [36].

210 In summary, we report here the first high-resolution structure of Acs1 homopolymers in a natively

211 polymerized state. These filaments form elaborate bundles in the nucleoplasm and cytoplasm of meiotic

212 yeast cells. Notably, nucleocytoplasmic filament bundles have previously been observed by others in

213   meiotic yeast cells [37] and were proposed to be actin-based/associated [38]. Using our novel FilamentID

214   approach, we characterized filament structure at higher resolution, which enabled the unambiguous

215   identification of the filament building blocks.

216   **Metabolites mediate Acs1 filament assembly to inhibit acetyl-CoA production**

217   Next, we set out to elucidate the functional relevance of Acs1 polymer formation. The first step towards

218   this goal was to determine the enzymatic state of filamentous Acs1. The metabolic reaction catalyzed

219   by Acs1 consists of two steps (Figure 5A). In the first step, Acs1 produces acetyl-AMP and diphosphate

220   from acetate and ATP. In the second step, the acetyl-AMP intermediate reacts with CoA to generate

221   acetyl-CoA [39]. During the enzymatic reaction, the large N-terminal domain (NTD) mediates the binding

222   of ATP substrate, whereas the small C-terminal domain (CTD) undergoes a large conformational change

223   to catalyze the second step of the reaction [36,40] (Figure 5B).

224   We found that Acs1 subunits in filaments have a conformation that is similar to the crystal structure of

225   the binary complex with AMP (PDB entry: 1RY2) (R.M.S.D. 1.30 Å, Figure S8A), which represents

226   the structure of the first step of the enzymatic reaction [36]. The acetyl-AMP intermediate could be

227   observed in the active site of the NTD and is located close to the catalytic residue K675 (Figure 5B and

228   S8B) [41]. Moreover, no acetyl-CoA product of the second step of the reaction was found in our

229   reconstructed map. In order to carry out the second step of the reaction, the Acs1 CTD has to undergo a

230   conformational change, which would result in a severe clash with the adjacent trimer layer shown by a

231   structural superposition with the bacterial ACS representing the open conformation of the second step

232   of the reaction (PDB entry: 1PG3; Figure 5C) [40]. Therefore, we propose that Acs1 in filaments catalyzed

233   the formation of acetyl-AMP. However, once in its filamentous form, Acs1 is sterically hindered by an

234   adjacent Acs1 trimer layer to produce the final product, acetyl-CoA.

235   To determine if the formation of acetyl-AMP is required for filament assembly, we mutated the key

236   residue K675 in the catalytic site and monitored the presence of filament bundles in spread spheroplasts

237   with cryoET. We did not observe any filament bundles in spreads from $acs1^{K675A}$ spheroplasts (n = 0/31),

238   while ~80% of the control strain ($ACS1^{WT}$) contained filament bundles (n = 24/30) (Figure 5E). Western

239   blotting using antibodies raised against Acs1 showed comparable protein expression (Figure 5F).

240   Moreover, we complemented this analysis by monitoring the cellular distribution of GFP-tagged Acs1.

241   We observed fluorescent rods and foci in the $ACS1^{WT}$-GFP strain but did not detect such structures in

242   the $acs1^{K675A}$-GFP mutant (Figure 5G). These data suggest that the catalytic activity of Acs1, in

243   particular the formation of the acetyl-AMP intermediate, is required for filament bundle formation.

244   Interestingly, we detected three additional densities at the interface between Acs1 trimer layers. These

245   extra densities likely correspond to metabolites, possibly ADP nucleotides (Figure 5D). Each putative

246   nucleotide binds to the surface of α helices in the Acs1 NTDs (Figure S8C). The putative nucleotides

247 are likely further stabilized via the α helix from the consecutive Acs1 NTD, which directly contacts the

248 positively charged residue R264 (Figure 5D). Additional interactions between two consecutive Acs1

249 trimer layers, especially salt bridges, are likely to contribute further to filament stability (Figure S8D).

250 To explore the role of the putative nucleotide in Acs1 filament assembly, we blocked the corresponding

251 binding site by mutating R264 to the bulky residue tryptophan. Strikingly, we no longer detected

252 elaborate filament bundles in spreads of meiotic $acs1^{R264W}$ spheroplasts (n = 0/30), even though the

253 expression level of Acs1^{R264W} was comparable to Acs1^{WT} (Figure 5E-F). Additionally, most meiotic cells

254 of $acs1^{R264W}$-GFP mutants contained only diffuse fluorescent signal (Figure 5G).

255 Overall, our structural and mutant analyses indicate that Acs1 polymerization is mediated by two

256 metabolites, acetyl-AMP bound in the catalytic pocket and a putative nucleotide bound at the filament

257 layer interface.

258 **The catalytic activity of Acs1 is required for sporulation and germination, whereas filament**

259 **formation is required for germination after prolonged dormancy**

260 Since *S. cerevisiae* harbors two acetyl-CoA synthetase isoforms, we wanted to understand under which

261 specific conditions Acs1 and its polymerization become critical. In an accompanying study, we

262 monitored global protein dynamics throughout meiosis using quantitative mass spectrometry and

263 observed that Acs1 expression is strongly upregulated at the onset of meiosis, when compared to

264 mitotically dividing cells (Figure 6A) [31]. Acs2, on the other hand, is highly expressed in mitotically

265 dividing cells, but downregulated during meiosis. Western blotting confirmed that the Acs1 level

266 increased in response to pre-meiotic starvation and increased even further approximately four hours after

267 induction of meiosis (Figure 6B).

268 In order to follow the formation of large Acs1 assemblies throughout the meiotic cell division program,

269 we monitored Acs1-GFP by fluorescent light microscopy. Meiotic cells, as well as spores, exhibited

270 fluorescent Acs1-GFP foci or rod-shaped signals (Figure 6C, S9). The number and intensity of Acs1-

271 GFP foci and rods appeared to increase throughout the meiotic program. Correlated light and electron

272 microscopy showed that Acs1-GFP foci indeed colocalized with polymerized Acs1-GFP, even though

273 filament length and filament bundling pattern seemed to be affected by the tag (Figure S10A-C).

274 Based on the presence of Acs1-GFP foci in meiotic cells as well as in spores, we then probed the role of

275 Acs1 in gametogenesis. We quantified sporulation efficiency in wild-type and different *acs1* mutant

276 strains upon gradual starvation (proliferating cells were starved in YPA before switching to SPM) or

277 acute starvation (proliferating cells were transferred from YPD directly into SPM). No significant

278 differences between the strains tested were observed upon gradual starvation (Figure 6D and S11). In

279 contrast, upon acute starvation, *acs1Δ* cells failed to sporulate (Figure 6E). This was also the case for

280 the catalytic point mutant $acs1^{K675A}$. Interestingly, the filament interface mutant $acs1^{R264W}$ sporulated

281 with comparable efficiency to the wild-type control $ACS1^{WT}$.

282 The experiments above indicate that the catalytic activity of Acs1 is required for efficient gametogenesis,

283 while filament formation is dispensable. However, they do not exclude that filament formation might be

284 required for spore viability, especially after prolonged periods of dormancy. We therefore used live cell

285 imaging to monitor spore germination and return to growth of spores of different ages. Gradual

286 starvation was used to induce sporulation and spores were kept in sporulation medium up to eight weeks

287 before inducing germination by switching to medium containing 2% glucose (Figure 6F). One day after

288 spore formation, most spores from all genotypes germinated within the 9 h of live cell imaging (Figure

289 6G). However, we noticed a delay in cell cycle re-entry for the $acs1^{K675A}$ and $acs1\Delta$ mutants, when

290 compared to the $ACS1^{WT}$ control. Interestingly, the $acs1^{R264W}$ spores germinated slightly faster than

291 $ACS1^{WT}$, indicating that filament formation might delay the germination of newly generated spores.

292 When spores were kept in sporulation medium for longer periods of time, we noticed a strong reduction

293 in the number of spores from $acs1^{K675A}$ and $acs1\Delta$ mutants strains that were able to germinate (Figure

294 6G). Remarkably, the filament interface mutant strain ($acs1^{R264W}$) also showed a steeper increase of time

295 required for re-entry into mitotic proliferation, when compared to the $ACS1^{WT}$ control. Moreover, after

296 prolonged times of dormancy, a large proportion of $acs1^{R264W}$ spores completely failed to germinate,

297 whereas the vast majority of $ACS1^{WT}$ spores re-entered proliferation efficiently (Figure 6G).

298 These data suggest that the polymerization of Acs1 into filaments is not required for the formation of

299 spores upon starvation. Moreover, filament formation, which inhibits catalytic function, may delay cell

300 cycle re-entry after short periods of starvation. However, failure to form Acs1 filaments results in

301 impaired return to growth after prolonged periods or dormancy. As such, it is likely that the inheritance

302 of meiotically-assembled Acs1 filaments plays a fundamental role in preparing spores for –

303 unpredictably – extended periods of dormancy.

304 **Acs1 polymerization is a general response to starvation and required for efficient recovery**

305 While monitoring the subcellular localization of Acs1-GFP, we noted that starved pre-meiotic cells

306 already contained Acs1-GFP foci (Figure 6C), suggesting that filament formation may occur as part of

307 a general response to the metabolic state, rather than being a meiosis-specific event. This would be

308 consistent with previous work showing that various GFP-tagged metabolic enzymes, including Acs1,

309 formed fluorescent foci upon nutrient depletion [10,12]. To test this hypothesis, we cultured haploid cells,

310 which cannot undergo meiosis, for 24 hours in YPA medium (containing acetate, a non-fermentable

311 carbon source, instead of glucose). CryoET imaging of spread spheroplasts revealed prominent Acs1

312 filament bundles as well as single Ald4 filaments that resembled those observed during meiosis (Figure

313 7A).

11

314   Having established that Acs1 filament formation also occurs when vegetative cells are starved in

315   medium containing acetate, we tested whether Acs1 played a role in return to growth after starvation,

316   independently from the meiotic cell division program. We cultured haploid cells for different periods of

317   time in medium with glucose (YPD medium) or in medium with acetate (YPA medium). The cells were

318   then transferred onto YPD and return to growth was monitored. As expected, after YPD starvation, wild-

319   type and Acs1 mutants recovered with similar efficiencies (Figure 7B), likely due to the functional

320   compensation by Acs2, which is upregulated in such conditions [42]. In contrast, after five days of YPA

321   starvation, significant defects in recovery were observed for the Acs1 catalytically deficient mutant

322   ($acs1^{K675A}$) as well as for the subunit interface mutant ($acs1^{R264W}$). Altogether, these data support a model

323   in which Acs1 filament formation is generally required for the ability of cells to return to proliferation

324   after prolonged periods of starvation.

325

DISCUSSION

Our multimodal cryoEM imaging approach on spread samples, termed FilamentID, revealed the structural organization of two novel types of filament assemblies composed of Ald4 and Acs1. Both metabolic enzymes are conserved across all domains of life. Acs homologs play a critical role in carbon metabolism and are also involved in the regulation of histone acetylation, which directly impacts chromatin structure and gene expression [43,44]. Ald homologs metabolize reactive aldehydes, and, as such, have important roles in detoxification and cell homeostasis [45]. Reflecting the functions in these central cellular processes, human Acs and Ald homologs are associated with disease. ACSS2 is highly expressed in cancer cells under conditions of metabolic stress [46], whereas reduced function of the mitochondrial ALDH2 has been linked to cancer predisposition, cardiovascular disease and, in 8% of the world population, alcohol intolerance [47]. From this perspective, it will be exciting to investigate whether polymer formation is an evolutionarily conserved aspect of Ald and Acs function, and whether polymerization may become altered in the context of disease. In the following paragraphs, we discuss the impact of our study on the understanding of Acs1 biology and metabolic enzyme filaments in general, as well as the methodological advances.

Context-specific enzyme polymerization: Acs1 subunit interfaces may sense the metabolic state of cells

Acetyl-CoA synthases and aldehyde dehydrogenases are protein families whose individual isoforms can be differentially regulated in terms of abundance and subcellular localization. Yeast Acs1 and Ald4 share a tight transcriptional repression by glucose [48,49]. Consistent with this notion, both proteins accumulate in starved pre-meiotic G0/G1 cells and throughout meiosis (Figure 6A) [31]. Furthermore, among several other metabolic enzymes, Acs1 and Ald4 were previously shown to accumulate as distinct foci in starved yeast cells, when tagged with GFP [10]. The mechanistic underpinnings of this behavior are currently unknown for most such enzymes. It has been proposed that low nutrient levels lead to cytoplasmic acidification and reduction in cell volume, eventually triggering widespread protein clustering, which leads to the transition of the cytoplasm from a fluid into a solid-like state [16,50,51]. Acs1 and Ald4 may therefore constitute isoforms of their respective enzyme families that have evolved the ability to polymerize in response to nutrient scarcity.

An elegant example of how a metabolic state can be sensed to trigger filament formation has been proposed for yeast CTP synthase. CTP synthase contains a histidine residue at the subunit interface that becomes protonated at low pH, leading to an increased affinity for the neighboring subunits [15]. Consistent with the idea that subunit interfaces can sense nutrient levels, our high-resolution structure of natively assembled Acs1 filaments revealed a metabolite, possibly ADP, at the interface of consecutive protomers (Figure 5D). Mutating the binding site at the interface abolished filament bundle

360   formation (Figure 5E, 5G). It is therefore tempting to speculate that sensing of the metabolic state of the

361   cell via ADP levels, which transiently increase during meiosis [52], may constitute a trigger for Acs1 to

362   polymerize. This underlines the critical role of subunit interfaces in the response to changes in nutrient

363   availability to tune oligomerization states. Besides this proposed mechanism, it is likely that other

364   regulatory layers play a role, including increased Acs1 expression levels and phosphorylation during

365   meiosis [31]. These aspects should be considered in future approaches aimed at reconstituting Acs1

366   filament formation *in vitro*.

367   **Acs1 polymerization is required for the recovery of chronologically aged dormant cells**

368   We propose a model, in which the essential catalytic function of Acs1, Acetyl-CoA synthesis, is carried

369   out at the onset of meiosis, when ATP production to support the vast biosynthetic needs of sporulation

370   is high [53], being shortly after followed by enzyme self-inhibition (Figure 7C). The upregulation of Acs1

371   under nutrient limiting conditions is accompanied by the polymerization of trimers into filaments, which

372   inactivates the enzyme. Should the inhibition of Acs1 be important for meiosis itself, one would expect

373   that sporulation or spore viability becomes compromised in mutants that specifically fail to form

374   filaments. We found that such a mutant (*acs1*^{R264W}) showed normal levels of sporulation (Figure 6E).

375   Remarkably, however, *acs1*^{R264W} failed to re-enter the cell cycle after prolonged periods of starvation-

376   induced dormancy (Figure 6G). Therefore, polymer formation appears to sustain the viability of dormant

377   spores that become chronologically old(er). More generally, Acs1 filaments also form in starved haploid

378   cells that cannot undergo meiosis and the ability of Acs1 to polymerize is critical for return to growth

379   after prolonged periods of starvation (Figure 7B).

380   How does Acs1 polymerization prime dormant/starved cells for efficient return to proliferation? We

381   envision several possible mechanisms: 1) The inactivation of Acs1 in polymers plays a role in lowering

382   acetyl-CoA levels as cells prepare to enter dormancy. This could, for example, ensure that histone

383   acetylation, which is a driver of chromatin openness and gene expression [54], remains low. 2) On the

384   other hand, Acs1 depolymerization after prolonged periods of starvation/dormancy, allows for the swift

385   generation of acetyl-CoA by the stored enzyme upon encountering favorable conditions. This provides

386   a two-fold advantage, namely no need for de novo Acs1/Acs2 synthesis, and, since Acs1 filaments are

387   acetyl-AMP-bound, acetyl-CoA can be produced without expending additional cellular ATP. 3) The

388   catalytic inactivation of Acs1, an abundant ATP-consuming enzyme, could help to preserve ATP levels

389   that are needed for minimal metabolism and for the re-entry into a metabolically active state. 4) Storage

390   of Acs1 via the formation of filament bundles could protect from autophagic degradation, which is a

391   highly active process during meiosis [55]. 5) Acs1 polymerization is part of a general cellular response to

392   solidify the cytoplasm. Such a transition was shown to increase mechanical stability and has been

393   proposed to protect from environmental stress [50,51].

394   An important remaining question is the molecular basis and relevance of Acs1 (and Ald4) to form

395   filaments that are organized in higher-order bundles and arrays (Figure 1A-C). These mesoscale

396   assemblies are likely established through lateral contacts of individual filaments. This idea is supported

397   by the observation that C-terminally GFP-tagged Acs1 formed only short filaments that co-localize in

398   unordered aggregates (Figure S10). The GFP-tag emanating from the filament surface likely disrupts

399   bundle formation and long-range polymerization. These findings underline the importance of integrating

400   cryoET imaging of untagged wild-type cells for a comprehensive understanding of metabolic enzyme

401   filaments across scales. Overall, our study will serve as a framework to understand how the

402   polymerization of metabolic enzymes and the formation of higher-order bundles may prime cells for

403   efficient recovery from dormancy.

404   **The FilamentID workflow can be adapted to various types of filaments**

405   Besides the possibility of analyzing the *in situ* structure of identified filament assemblies, cryoET is a

406   powerful method to discover new cellular ultrastructures in a range of cellular states, organisms, and

407   tissues[21,22]. The *de novo* identification of such structures *in cellulo*, however, is extremely challenging,

408   as it requires the determination of reconstructions by sub-tomogram averaging at a resolution of typically

409   <4 Å to unambiguously identify unique amino acid sequences. Recent successful examples were enabled

410   by the combination of 1) highly abundant target complexes (e.g. ribosomes) and 2) particularly thin

411   samples for imaging, for instance skinny bacteria [56,57] or cryoFIB-thinned cells [58,59]. An alternative

412   approach to sub-tomogram averaging is to determine high-resolution structures via single-particle

413   cryoEM, however, this is typically done on purified complexes. Integrated with advanced computational

414   analyses, *de novo* identification is also feasible with rather heterogeneous samples [60-62]. Any purification,

415   however, can lead to disassembly of the structure of interest.

416   The FilamentID workflow (Figure 2) combines complementary imaging modalities on gently lysed

417   cells/organelles and has three major advantages over the above conventional approaches: 1) FilamentID

418   needs no prior sample knowledge; 2) FilamentID can be applied to targets of rather low abundance and

419   heterogeneity at the superstructural level; and 3) FilamentID sample preparation does not require time-

420   consuming cryoFIB milling or purification optimizations. Limitations of the technique are that 1) the

421   targeted single-particle cryoEM data collection needs to be guided to areas of interest (target complexes

422   need to be visible at low magnification); and 2) membrane integrity and cellular context is lost due to

423   the spreading.

424   In the present study, FilamentID could unambiguously pinpoint the composition of two different types

425   of filamentous assemblies. We note, however, that we detected other types of filaments in cryo-

426   tomograms of spread yeast cells (Figure S5B). In the future, the workflow could be adapted to study

427   various culturing conditions, distinct developmental programs, different cell types, and diverse

428   organisms.

AUTHOR CONTRIBUTIONS

J.H. performed the sample preparations for cryoEM/cryoET with the help of F.W.; J.H. and J.X. performed cryoET data collection and analysis; J.H. and J.X. collected cryoEM data; J.X. reconstructed the cryoEM maps and determined the structures; R.W. provided MS data and analysis; J.H., R.W., L.I. D.V. and A.H. generated yeast strains. R.W. and A.H. performed western blotting experiments; J.H. and R.W. performed sporulation efficiency assays; L.I. performed immuno-florescence imaging. J.H. performed correlative cryoLM and cryoET imaging; J.H. did starvation recovery assays; D.V. performed germination assays and analyzed the data with J.H.; J.M. and M.P. conceived and supervised the project; J.H., J.X., J.M. and M.P. wrote the manuscript with input from all authors.

DECLARATION OF INTERESTS

The authors declare no competing interests.

DATA AND MATERIAL AVAILABILITY

The EMDB entries for the cryo-EM density maps of the Acs1 and Ald4 filaments reported in this paper are EMD-XXXXX (Ald4) and EMD-XXXXX (Acs1). The PDB entries for the corresponding atomic models reported in this paper are XXXX (Ald4) and XXXX (Acs1).

The EMDB entries for the tomograms showing Ald4 or Acs1 filament bundles are EMD-XXXXX (Ald4 filments in mitochondria; meiotic *in cellulo*), EMD-XXXXX (Acs1 filaments in the nucleus; meiotic *in cellulo*), EMD-XXXXX (Acs1 filaments in the cytoplasm; meiotic *in cellulo*), EMD-XXXXX (Ald4 filaments in purified mitochondria from meiotic cells), (Acs1 filaments in spread spheroplasts from meiotic cells), and EMD-XXXXX (Acs1 and Ald4 filaments in spread spheroplasts from starved cells).
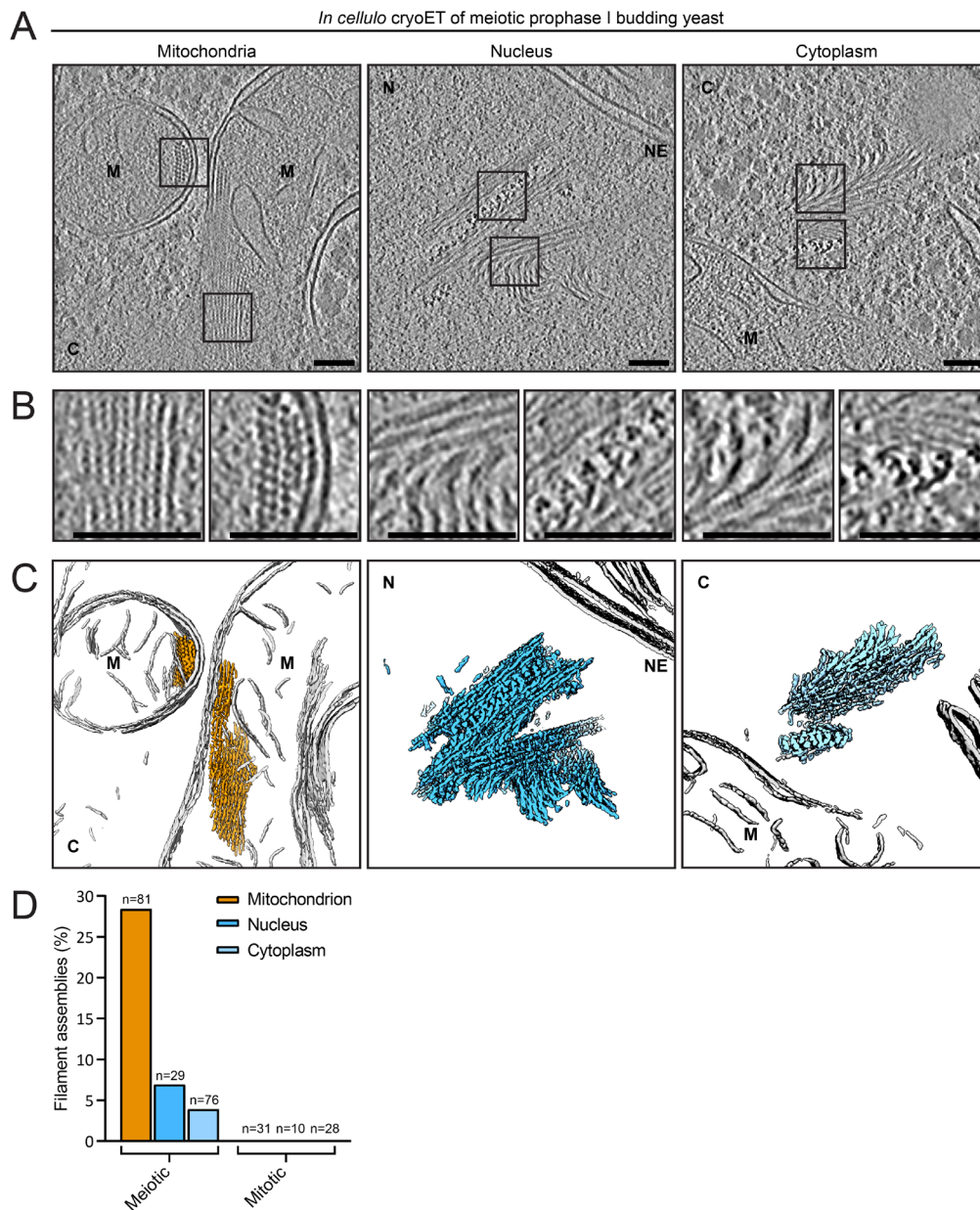
FIGURES

Figure 1. Filament assemblies form in the mitochondria, nucleus, and cytoplasm of meiotic yeast cells. See also Figure S1.

(**A**) Slices through cryo-tomograms of FIB-milled meiotic prophase I budding yeast cells with filament assemblies in the mitochondria, in the nucleus, and in the cytoplasm. Shown are projections of 9.14 nm (mitochondria) and 8.68 nm (nucleus and cytoplasm) thick slices. Cells were collected from a *ndt80Δ* strain arrested in prophase I, 8 h post induction of meiosis. M: mitochondrion, C: cytoplasm N: nucleus, NE: nuclear envelope. Scale bars: 100 nm.

465 **(B)** Magnified views of cryo-tomograms shown in (**A**). Note that the top views of single filaments
466 display a round shape for mitochondrial filaments, whereas the nuclear and cytoplasmic filaments have
467 a triangular shape. Scale bars: 100 nm.

468 (**C**) Segmentation models of cryo-tomograms in (**A**) showing filament arrays and bundles.
469 Mitochondrial filaments (orange), nuclear filaments (blue), and cytoplasmic filaments (light blue) are
470 highlighted. Organelle membranes are colored in gray.

471 (**D**) Filament assemblies in the different cellular compartments are observed in meiotic but not in
472 mitotically dividing cells. Meiotic mitochondria (n = 81), nuclei (n = 29), and cytoplasm (n = 76) and
473 mitotic mitochondria (n = 31), nuclei (n = 10), and cytoplasm (n = 28) were analyzed. The fraction (%)
474 of mitochondria, nuclei, and cytoplasm containing the main types of filaments described in (**A-C**) is
475 indicated for each cellular context. Numbers for analyzed compartments (n) represent cumulated results
476 from at least two independent experiments.

477

478
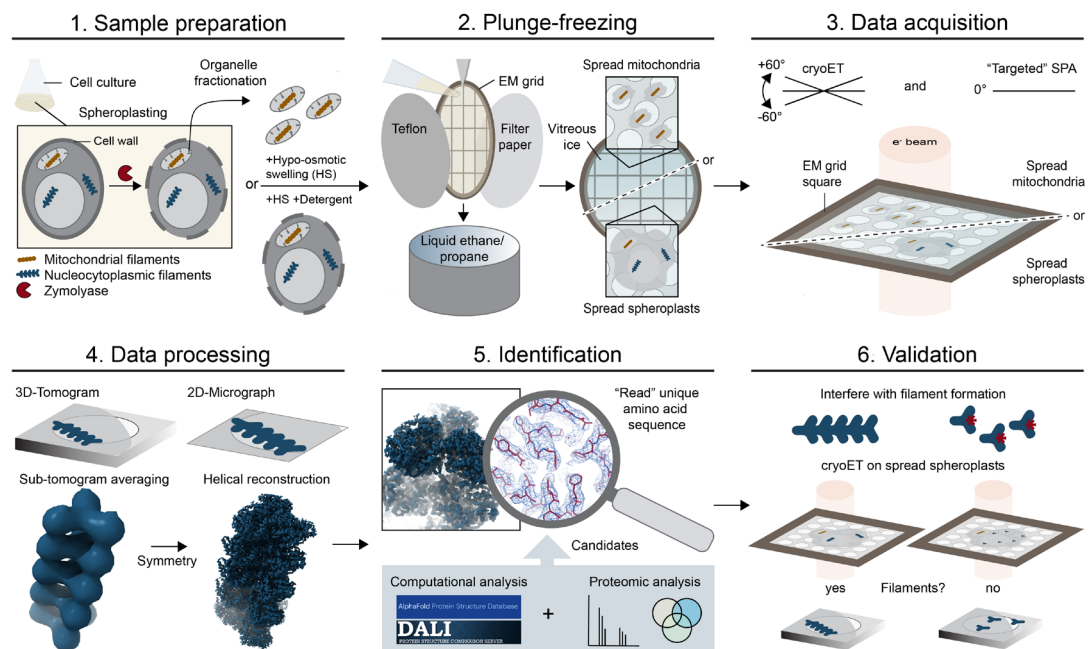
Figure 2. FilamentID: a workflow to identify cellular filaments of unknown molecular composition. See also Figure S2/S5.

Schematic workflow to IDentify the composition of Filament assemblies (FilamentID) observed *in cellulo*. Key steps (1-6): (1) Sample preparation: cells are spheroplasted by digesting the cell wall with Zymolyase. Depending on the subcellular localization of the filaments, either mitochondria are purified and spread onto EM grids, or entire cell spheroplasts are spread onto EM grids by hypo-osmotic swelling and the addition of detergent. (2) Plunge-freezing: samples are vitrified by plunge-freezing. (3) Each sample is imaged by recording tilt series for cryoET, as well as 2D projection images for single-particle cryoEM. (4) Data processing: the cryoET data are used to generate sub-tomogram averages to determine filament symmetry. Subsequently, single-particle data are used to generate high-resolution maps by helical reconstruction, based on the initial symmetry information determined by cryoET. (5) Identification: information from computational analysis is used to identify the filament component(s). Depending on the level of resolution obtained, complementary information from proteomics can be used to narrow down candidates. (6) Validation: candidate gene(s) are deleted and cryoET is used to verify the impact on filament structure. In addition, the structural information obtained is used to guide the perturbation of filament formation by the introduction of specific point mutations. Note: it also would have been possible to identify the mitochondrial filaments without the mitochondrial purification in step 1; however, the mitochondrial purification step significantly simplifies steps 3-6. For simplicity, in steps 4-6 only the nucleocytoplasmic filament is shown.

498

499
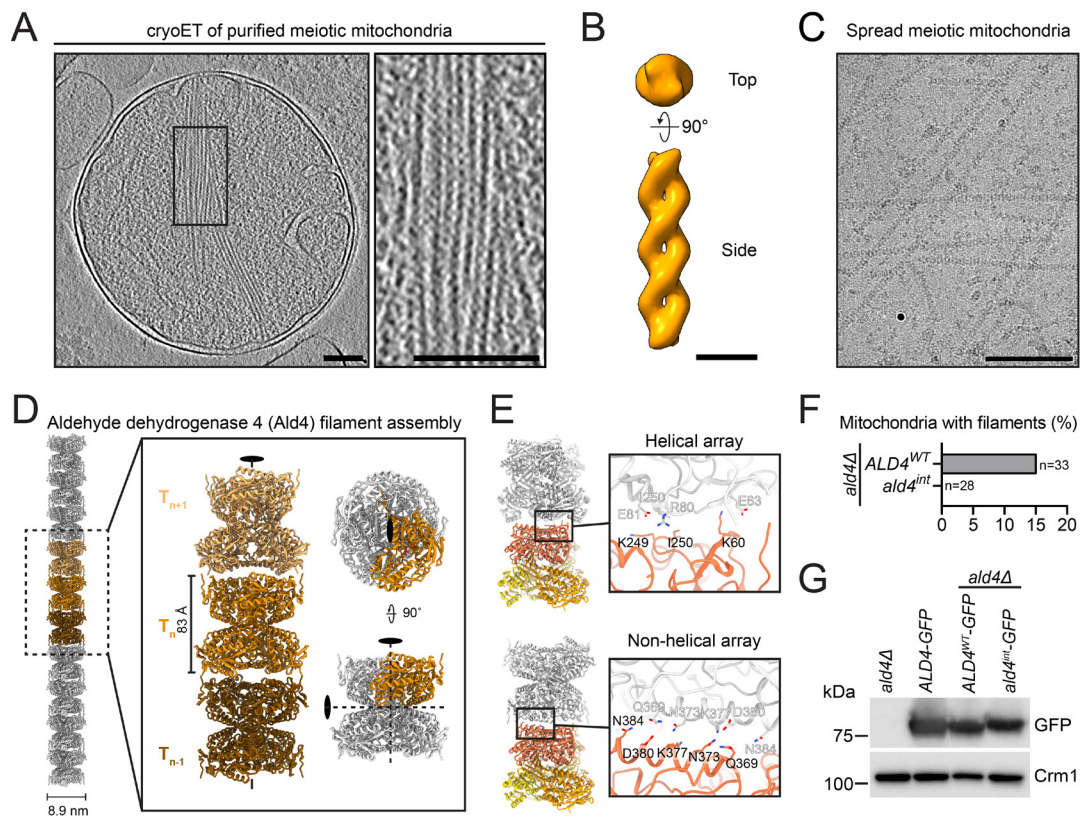
Figure 3. The conserved mitochondrial aldehyde dehydrogenase Ald4 polymerizes into filaments.
See also Figure S2-S4.

(**A**) Slice through a cryo-tomogram of purified mitochondria. Note that straight filament arrays can cross the entire width of the mitochondrion as depicted. Magnified view of the boxed area is shown on the right. Cells were collected from a *ndt80Δ* strain arrested in prophase I, 6 h post induction of meiosis. Shown are projections of 5.5 nm thick slices. Scale bars: 100 nm.

(**B**) Sub-tomogram averaging of filaments from purified meiotic mitochondria shown in (**A**) reveals a two-fold symmetry. Shown are top and side views. Scale bar: 10 nm.

(**C**) Purified mitochondria in (**A**) were spread and imaged by cryoEM. A representative micrograph with individual filaments observed in spread meiotic mitochondria is shown. Scale bar: 100 nm.

(**D**) Structural model of Ald4 in a filamentous form. Left: stacked array of one Ald4 filament, in which three consecutive Ald4 tetramers are colored in different shades of orange. Right: magnified view of the central three Ald4 tetramers on the left. The top and side views of the ribbon diagram of the central Ald4 tetramer are shown on the right, where a single Ald4 subunit is colored orange. The two-fold axis of Ald4 is represented by an ellipse.

(**E**) Ribbon diagrams showing the putative interfaces between two consecutive Ald4 tetramers in helical (top) and non-helical (bottom) arrays. The subunits of one Ald4 tetramer are colored in different shades

517   of orange, while the other Ald4 tetramer is colored white. The detailed interface contacts are shown on

518   the right, where the side chains of putative residues mediating contacts are labeled and shown in stick

519   diagrams.

520   (**F**) The Ald4 interface shown in (**E**) is needed for filament formation. Purified mitochondria from

521   meiotic cultures (6 h after induction of meiosis) of the indicated genotypes were analyzed by cryoET as

522   described in more detail in Figure S4E. Shown are percentages of mitochondria containing filaments

523   and the total number of mitochondria (n) analyzed for each genotype are indicated.

524   (**G**) Ald4 interface mutations do not affect protein stability. Western blot analysis from haploid cell

525   cultures collected after 24 h in YPA media. Ald4-GFP expression levels were probed with anti-GFP

526   antibodies and compared in strains with the indicated genotypes. Crm1 was used as protein

527   normalization control.

528
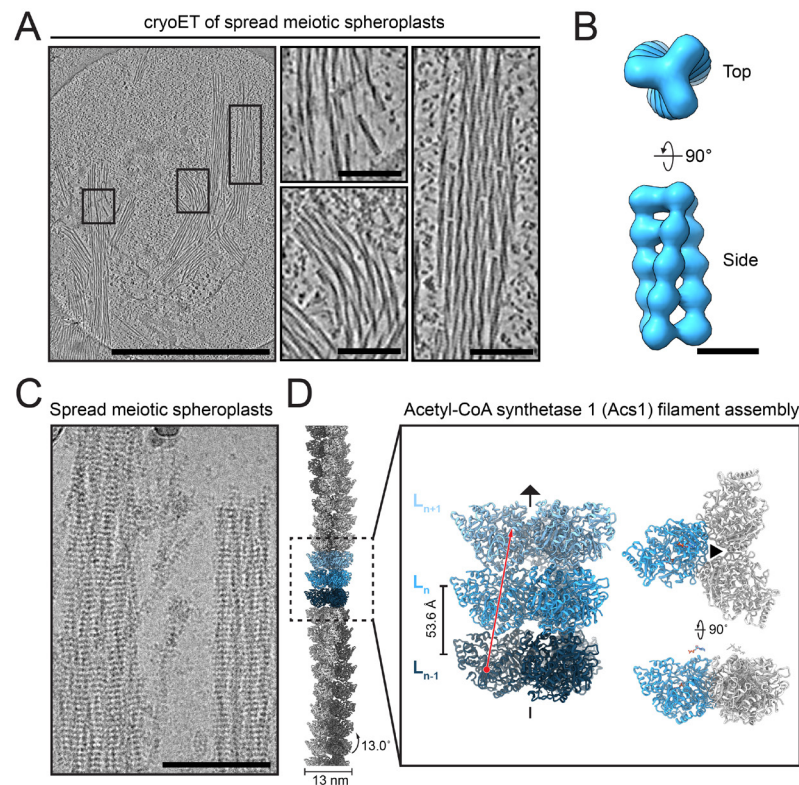
Figure 4. The conserved acetyl-CoA synthetase Acs1 forms filament assemblies in the nucleus and the cytoplasm. See also Figure S5-S7.

(**A**) Slice through a cryo-tomogram of spread meiotic yeast spheroplasts enable a detailed view of the nucleocytoplasmic filaments assemblies observed in Figure 1A. Magnified views of the boxed areas highlight single filaments as well as straight and bent bundles. Cells were collected from a *ndt80Δ* strain arrested in prophase I, 8 h post induction of meiosis. Shown are projections of 9.14 nm thick slices. Scale bars: 1 μm and 100 nm for magnified views.

(**B**) Sub-tomogram averaging of filaments from yeast spheroplasts shown in (**A**) reveals a three-fold symmetry with a ladder-like repeat. Shown are top and side views. Scale bar: 10 nm.

(**C**) Representative cryoEM micrograph of filament bundles from spread meiotic yeast spheroplasts as shown in (**A**). Scale bar: 100 nm.

(**D**) Structural model of Acs1 in its filamentous form. Left: Helical array of triple-helical Acs1 filament. A single helical strand is highlighted in dark gray and three consecutive layers are colored in different shades of blue. Right: Magnified view of the central three layers on the left. The single helical strand is marked with a red arrowhead. The side and top view of the ribbon diagram of the central Acs1 trimer are shown on the right, where a single Acs1 subunit is colored in blue. The three-fold axis of the Acs1 trimer is represented by a triangle.

547
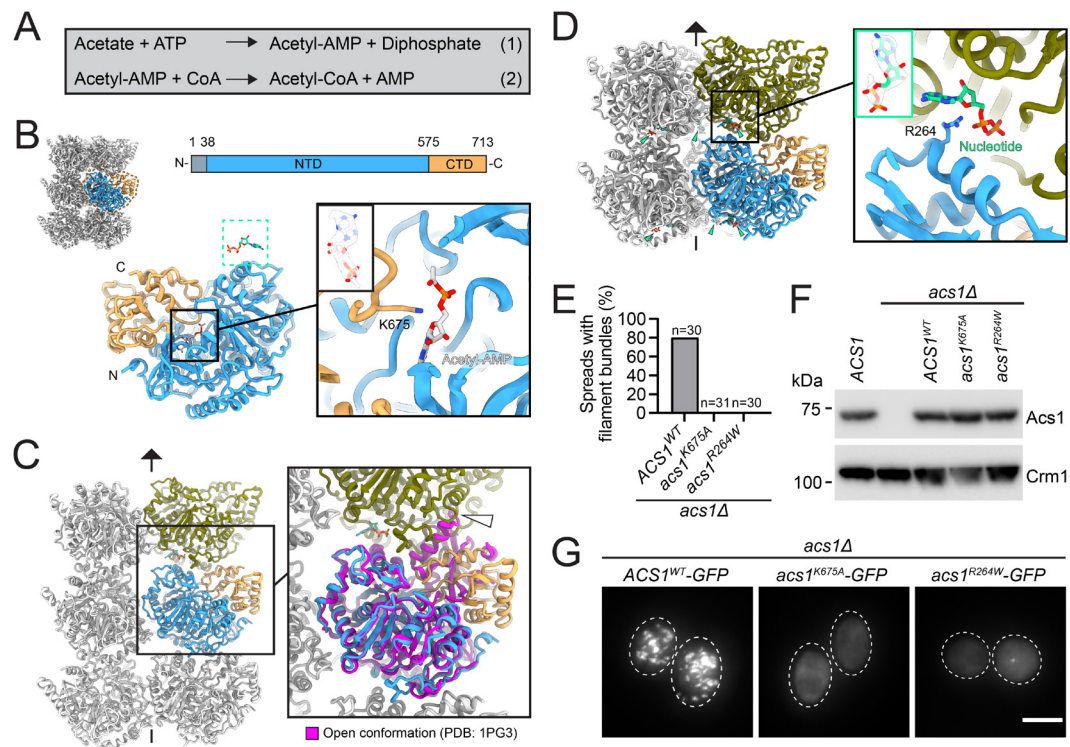
Figure 5. Metabolites mediate Acs1 filament assembly to inhibit acetyl-CoA production. See also Figure S8.

(**A**) Acs1 uses acetate and ATP to produce acetyl-CoA in a two-step reaction. In the first step, an acetyl-AMP intermediate is formed, and diphosphate is released. In a second step, acetyl-AMP reacts with CoA to produce acetyl-CoA with the release of AMP [39].

(**B**) Ribbon and stick diagrams showing two types of metabolites bound to Acs1 in the filament. Top left: the helical array of three Acs1 layers, where one subunit is colored and highlighted with a dashed line. Top right: Scheme showing the overall Acs1 domain organization, where the N-terminal large domain (NTD) and the C-terminal small domain (CTD) are colored blue and orange respectively. The flexible N-terminal part, which is not resolved in the structure, is colored grey. Bottom-left: the structural model of one Acs1 subunit with two metabolites bound (acetyl-AMP: gray; nucleotide (potentially ADP): green). The position of the nucleotide is highlighted with a green dashed box and the details are shown in panel (**D**). Bottom-right: Magnified view showing the contacts between acetyl-AMP and Acs1. The side chain of the residue in the catalytic center (K675) is shown in stick diagram, while the corresponding densities around acetyl-AMP are transparent.

(**C**) Ribbon diagrams illustrating the predicted structural clashes that prevent the second step in acetyl-CoA synthesis when Acs1 is in a filamentous form. Left: helical assembly of three Acs1 trimer layers, where one Acs1 subunit is color-coded as in (**B**) and one subunit from the adjacent trimer layer is colored olive. Right: structural superposition of one Acs1 subunit with CoA-bound bacterial ACS (PDB entry:

23

567   1PG3) [40]. Note the severe steric clashes (highlighted with white arrowhead) between the bacterial

568   homolog (magenta) and the Acs1 molecules in the adjacent filament layer (olive).

569   (**D**) Ribbon and stick diagrams showing the metabolic nucleotide (potentially ADP) bridging two Acs1

570   adjacent layers. Left: the structure of Acs1 subunits from two adjacent layers. The color code of two

571   subunits matches panel (**C**). Right: Magnified view showing the contacts between the nucleotide (green)

572   and Acs1 subunits. The side chain of the residue binding to the nucleotide (R264) is shown in stick

573   diagrams. The corresponding densities around the nucleotide are shown in transparent.

574   (**E**) No filament bundles are detected in point mutation strains of the residues shown in (**B**) and (**D**).

575   Spread meiotic yeast spheroplasts (6 h after induction of meiosis) for the indicated genotypes were

576   analyzed by cryoEM as described in more detail in Figure S7D. Shown are percentages of spreads

577   containing Acs1 filament bundles in EM images and the total number of spreads (n) analyzed for each

578   genotype are indicated.

579   (**F**) Acs1 point mutations do not affect protein stability. Western blot analysis from meiotic cell cultures

580   collected 6 h after induction of meiosis. Acs1 expression levels were probed with an anti-Acs1 antibody

581   and compared in strains with the indicated genotypes. Crm1 was used as protein normalization control.

582   (**G**) Fluorescent rods and foci formation is disrupted in *ACS1* point mutation strains C-terminally tagged

583   with GFP. Shown are representative maximum intensity projections of the Acs1-GFP signal expressed

584   from the endogenous promotor for the indicated genotypes. Cells were collected 6 h after induction of

585   meiosis. Cell walls are indicated with a dashed white line. Scale bar: 5 μm.

586

587
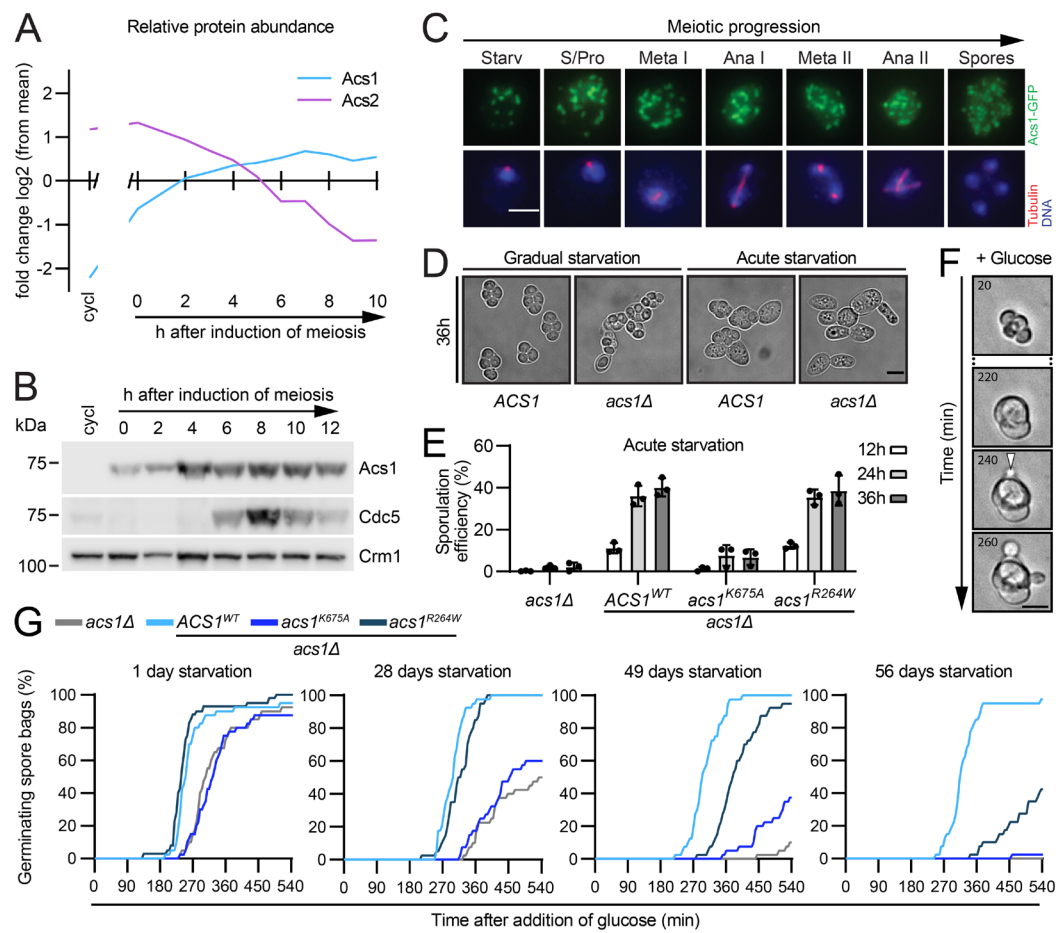
Figure 6. The catalytic activity of Acs1 is required for sporulation and germination, whereas filament formation is required for germination after prolonged dormancy. See also Figure S9-S11.

(A) Dynamic changes in the relative expression of Acs1 and Acs2 monitored by quantitative proteomics, extracted from [31]. Samples from cycling mitotic cultures (cycl; in YPD medium), and samples collected at the indicated time points after induction of meiosis from G0/G1 have been analyzed. The plotted values represent the log2 fold change in each sample compared to the average peptide/protein expression from all samples.

(B) Acs1 is highly expressed throughout meiosis. Western blot analysis of Acs1 in exponentially growing cycling cultures (cycl; in YPD medium), and at the indicated time points after induction of meiosis, in SPM medium. Cdc5 expression was used as a marker of meiotic progression whereas Crm1 serves as protein normalization control.

(C) Acs1-GFP forms foci and rods throughout gametogenesis. Acs1-GFP expressed from the endogenous promoter was analyzed by immunofluorescence using anti-GFP antibodies. Spindle morphology and DNA were visualized using anti-α-tubulin antibodies and DAPI respectively. The experiment shown is representative for two independent experiments. Scale bar: 3 μm.

25

(**D**) Acs1 is needed for efficient sporulation after acute starvation. Yeast strains with the indicated genotypes were induced to enter meiosis by transfer from YPD to SPM (acute starvation), or by transfer from YPD to YPA to SPM (gradual starvation). Shown are representative images of the sporulation efficiency 36 h after transfer to SPM medium. Note that in acutely starved cell cultures of an *acs1Δ* strain no ascospore formation was observed. Quantification of the sporulation efficiency is shown in Figure S11. Scale bar: 5 μm.

(**E**) The catalytic activity of Acs1 is needed for efficient sporulation, whereas filament formation is dispensable. Yeast strains with the indicated genotypes were induced to sporulate as in (**D**) under acute starvation conditions. The efficiency of ascospore formation was quantified by assessing the morphology of 200 cells from three independent experiments after 12, 24, and 36 h in SPM. Ascospore formation was considered successful if at least two spores were enclosed by a spore wall. Plotted values show the mean ± SD.

(**F**) Live cell imaging of ascospore germination. Strains shown in (**G**) were induced to sporulate under gradual starvation conditions, as described in (**D**). Mature spores were then induced to germinate by exchanging the sporulation medium (SPM) to glucose-rich medium (SC + 2% Glucose). Light microscopy DIC images were collected every 5 min to follow the initial bud formation, which was considered as the initial point of re-entry into the cell cycle. Example images depict the key morphological changes that occur after transfer of the spores to glucose-rich medium, with bud formation marked by the white arrowhead. Scale bar: 5 μm.

(**G**) Acs1 filament formation is needed after prolonged dormancy. Ascospore germination was analyzed as described in (**F**) for strains with the indicated genotypes, after cells were cultured for 1, 28, 49, and 56 days in SPM medium. 40 ascospores per genotype and condition were imaged for cell cycle re-entry. Live cell imaging was performed for a total duration of 540 min (9 h) after glucose addition.
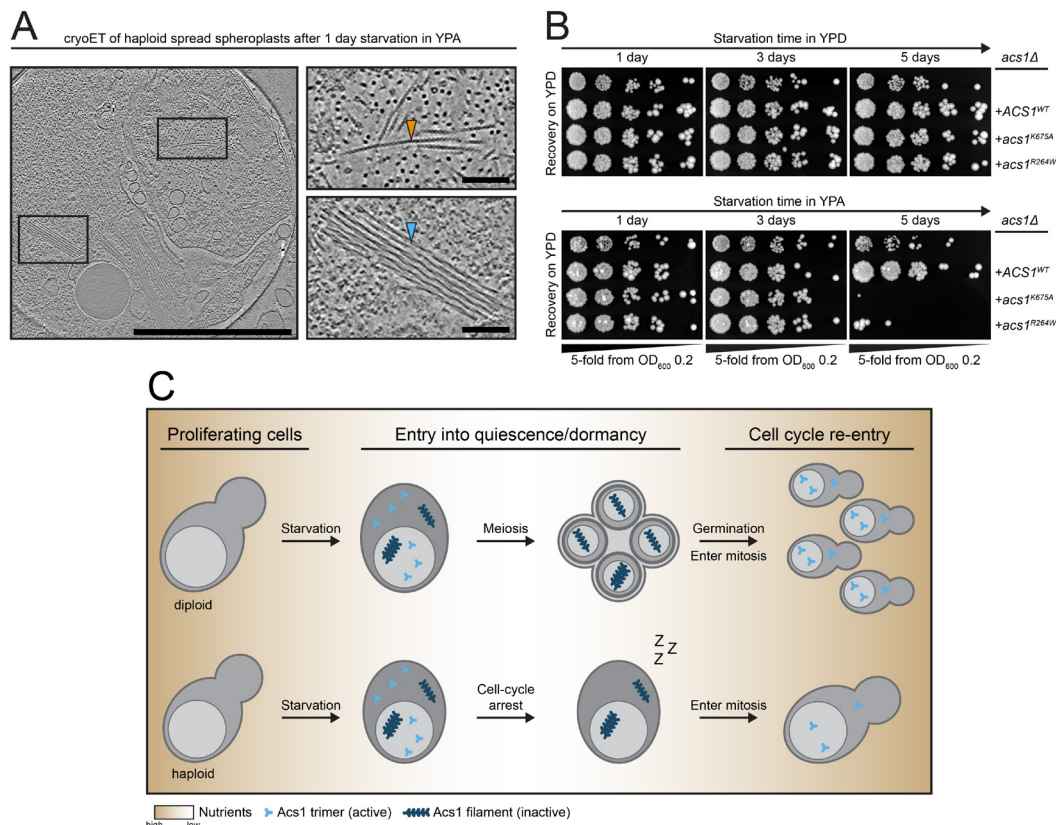
Figure 7. Acs1 polymerization is a general response to starvation and required for efficient recovery.

(**A**) Acs1 and Ald4 form filaments also upon starvation independently from meiosis. Haploid yeast cells, which are unable to enter meiosis, were starved for 1 day in YPA, spread onto EM grids, and processed for cryoET. Shown is a 9.02 nm thick slice through a cryo-tomogram with magnified views on the right. Orange arrowhead points to single Ald4 filament whereas the blue arrowhead points to an Acs1 filament bundle. Scale bars: 1 µm and 100 nm for magnified views.

(**B**) Acs1 filaments are needed for efficient recovery after starvation. Shown is a cell spotting assay for the indicated genotypes. Cells were incubated for 1, 3, or 5 days in YPD or YPA medium before fivefold serial dilutions were spotted on YPD plates. Note that after five days in YPA medium, deletion strains complemented with *acs1*^{K675A} and *acs1*^{R264W} almost completely failed to recover. The experiment shown is representative for two independent experiments.

(**C**) Model of Acs1 filament function. Starvation triggers entry into quiescence/dormancy via meiosis. In the process, Acs1 expression is upregulated to promote acetyl-CoA production, which is required for meiosis. Shortly after meiotic entry, Acs1 polymerizes and forms filament bundles that are inherited by spores. In the filamentous form, Acs1 is inactive and acetyl-AMP-bound, unable to carry out the second step in acetyl-CoA synthesis. After long periods of dormancy, the stored Acs1 is required for return to

27

645   proliferation. A similar mechanism operates in haploid cells to enable the return to growth from

646   prolonged periods of starvation.

647

STAR METHODS

Experimental model and subject details

All strains used in this study are SK1 derivatives and the detailed genotypes are described in Table S2. The following alleles have been described previously: *ndt80Δ, Zip1-(700)-GFP* [63,64]. Gene deletions were introduced by PCR-based amplification of cassettes from the yeast knock-out collection [65]. Synthetic *ALD4^{WT}* or *ald4^{int}* (Lys60Glu, Lys249Glu, Ile250Ala, Gln369Ala, Asn373Ala, Lys377Ala, Asp380Ala, Asn384Ala) constructs including 500 base pairs (bp) upstream of ATG and 500 bp downstream of the terminator were cloned into the plasmid Yiplac128 (pML764) using HindIII and EcoRI restriction sites. The resulting plasmids (pML767 and pML776) were used to reconstitute an *ald4Δ* strain by the integration of the respective linearized vector variant into the promotor region of *ALD4* using SmaI. In all strains carrying *ACS1* variants, a synthetic *ACS1^{WT}-6xHIS-6xFLAG* gene sequence construct including 301 bp upstream of ATG and 81 bp downstream of the terminator was cloned into the plasmid pYIplac211 (pML533) using HindIII and EcoRI restriction sites. Plasmids carrying *acs1^{K675A}* (pML624) or *acs1^{R264W}* (pML619) were generated by site-directed mutagenesis of pYIplac211-*ACS1-6xHIS-6xFLAG* (pML606). Reconstitution of *acs1Δ* strains with *ACS1^{WT}* or with the *acs1* point mutants were performed by integration of the respective linearized vector variants into the promotor region of *ACS1* using Bsu36I. For C-terminal PCR-based tagging of chromosomal genes or tag exchange with yeast enhanced GFP (referred to in the text as GFP) cassette was amplified from a plasmid (pML100, Gift from Wolfgang Zachariae) with 50 bp overhangs homologous to 50 bp up- and downstream of the STOP codon [66]. To remove C-terminal tags, a cassette from pML702 with 50 bp overhangs at the C-terminus including the STOP codon was used. DNA cassettes were transformed into SK1 yeast strains using standard protocols.

Method details

Generation of diploid strains and meiotic time courses

Meiotic time courses were performed as previously described [23,24]. In brief, haploid cells with opposite mating types were mated on YPD [1% (w/v) yeast extract, 2% (w/v) peptone, 2% (w/v) dextrose]. Diploid cell colonies were then selected on YPG [1% (w/v) yeast extract, 2% (w/v) peptone, 2% (v/v) glycerol] plates for 48 h at 30 °C. Several colonies were picked and expanded on YPD plates for two times 24 h at 30 °C to form a lawn covering the whole plate. Afterwards, cells were inoculated in pre-sporulation medium [YPA, 1% (w/v) yeast extract, 2% (w/v) peptone, 2% (w/v) potassium acetate] at OD_{600} ~0.3 and grown for 15 h at 25 °C or for 11 h at 30 °C, washed once in sporulation medium [SPM, 2% (w/v) potassium acetate] and inoculated at OD_{600} ~3.5 into SPM. This time was defined as t = 0 h

680   for all meiotic time courses. Cells were then sporulated at 30 °C and samples were taken at specific time

681   points post transfer to SPM.

682   **Sporulation efficiency**

683   To assess sporulation efficiency, cells were inoculated in YPA to OD_{600} ~0.3 and grown for 15 h at 25

684   °C, washed once in SPM, and inoculated into SPM to OD_{600} ~3.5. For the acute starvation procedure,

685   cells were directly inoculated into SPM after expansion on YPD plates. An aliquot of cell suspension

686   was collected after 12 h, 24 h, and 36 h in SPM and stored at -20 °C prior to light microscopy imaging.

687   Samples were imaged with standard light microscopy systems. Areas with ascospores and cells were

688   randomly picked, and Z-stacks were recorded in the Brightfield channel. Ascospores and cells were

689   manually scored using Fiji [67]. 100-200 ascospores or cells were counted in three independent

690   experiments. Ascospore formation was considered successful if the ascus contained at least two spores

691   enclosed by a separate spore wall. Data analysis was performed in Excel (Microsoft) and Prism (version

692   9.2.0 for Windows; GraphPad) software.

693   **Yeast spore germination imaging**

694   Sporulation cultures generated as described above were incubated for up to 56 days at 30 °C in SPM

695   medium supplemented with Ampicillin (50 μg/ml). Every three days, fresh Ampicillin was added. For

696   life cell imaging, samples were adjusted to an OD_{600} ~1.7 in conditioned SPM before they were put in

697   Concanavalin A (in 1M $MnCl_2$, 1x PBS) coated imaging chambers [Nunc™ Lab-Tek™ II Chambered

698   Coverglass, 8 Well, 1.5 Borosilicate Glass (LifeTech Cat 155409)]. After 3 min of incubation at RT,

699   chambers were washed with conditioned SPM before synthetic medium [SC, 0.17% (w/v) yeast nitrogen

700   base w/o ammonium sulphate and amino acids, 0.5% (w/v) ammonium sulphate, 1.1% casamino acids,

701   0.0055% (w/v) for adenine, tyrosine, uracil, tryptophane and leucin in H_2O] w/o glucose was added.

702   Right before imaging, SC w/o glucose was exchanged with SC containing 2% (w/v) glucose. Live-cell

703   imaging was performed on a DeltaVision Ultra Epifluorescence Microscope equipped with an Olympus

704   UPlanXApo 40x/0.95 Corr objective, a sCMOS camara (pco.edge 4.2) and a full environmental chamber

705   at 30 °C. 8 μm z-stacks in the DIC channel were collected every 5 min for a total duration of 9 h on pre-

706   selected regions. Additionally, a UV blocking filter was applied.

707   Movies were analysed with Fiji imaging software. Single ascospores containing at least three visible

708   spores enclosed by a separate spore wall were tracked over the entire movie. The time of initial cell

709   cycle re-entry was defined as the appearance of the first budding spore of an ascus. 40 ascospores per

710   genotype were inspected for each time point. Germination curves were generated in Excel (Microsoft)

711   and Prism (version 9.2.0 for Windows; GraphPad) software.

Yeast spot assays

Haploid yeast cells were cultured in liquid YPD over night at 30 °C. In the morning, cells were diluted and inoculated at $OD_{600} \sim 0.1$ in YPD or $OD_{600} \sim 0.2$ in YPA medium supplemented with Ampicillin (50 µg/ ml) and incubated at 30 °C. Every three days, cell cultures were supplemented with fresh Ampicillin. For the starvation recovery spot assay, cells were harvested for each time point, washed once in H_2O and spotted on YPD plates as 5-fold serial dilutions starting from $OD_{600} = 0.2$. YPD plates were incubated for 48 h at 30 °C before they were imaged with a ChemiDoc Imaging System (BioRad).

Protein analyses by western blotting

Samples were processed as described previously (Matos et al., 2008). In short, cell pellets were disrupted in 10% TCA using glass beads on a FastPrep-24 (MP Biomedicals) running two cycles of 40 s (6.5 m/s). The protein precipitates were resuspended in 2X NuPAGE sample buffer and neutralized with 1M TrisBase at a 2:1 ratio (v/v), boiled at 95°C for 10 min and cleared by centrifugation for another 10 min. The relative protein concentration was assessed using the Bio-Rad protein assay. Protein samples were separated on NuPAGE 3-8% Tris-Acetate gels (Invitrogen) and transferred onto Amersham Hybond 0.45 µm PVDF membranes. For immunoblotting the following antibodies were used: mouse anti-GFP (1:2000, 11814460001 Roche), mouse anti-Cdc5 (1:2500, clone 4F10 MM-0192-1-100 MédiMabs), rabbit anti-Acs1 (1:5000, this publication), rabbit anti-Crm1 (1:5000, Onischenko E. et al., 2009). The following secondary HRP conjugated antibodies were used: 1:5000 goat anti-mouse immunoglobulin (P0447 Agilent) and 1:5000 swine anti-rabbit immunoglobulin (P0399 Agilent).

FACS analysis of DNA content

Cellular DNA content was determined as described previously [68]. 1 ml of meiotic cell culture was fixed in 70% (v/v) ice cold EtOH before cells were washed in 50 mM Tris-HCl pH 7.5 and resuspended in 500 µl 50 mM Tris-HCl pH 7.5. RNA was digested o/n or for at least 4 h at 37 °C by adding 2 µl RNase (100 mg/mL) (Roche). Cells were washed in FACS buffer (200 mM Tris-HCl pH 7.5, 211 mM NaCl, 78 mM $MgCl_2$), resuspended in 500 µl FACS buffer containing 50 µg/ml propidium iodide and briefly sonicated. An aliquot of 40-60 µl was diluted in 1 ml of 50 mM Tris-HCl pH 7.5. Propidium iodide-stained DNA content was measured on a flow cytometer (FACSCalibur or LSRFortessa, Becton Dickinson). The cytometer data was analyzed using FlowJo software (Becton Dickinson).

Fluorescence light microscopy

Immunofluorescence stainings were performed as previously described [69,70]. The following primary antibodies were used: rabbit anti-GFP (1:600, a gift from Wolfgang Zachariae), rat anti-α-tubulin (1:600, Biorad MCA78G). Secondary antibodies coupled to Alexa 555 and Alexa 488 were used for detection (1:300, Invitrogen). DNA was stained with 4',6-diamidino-2-phenylindole (DAPI). Images were

745 acquired on a Zeiss Axio Imager M2 equipped with a 63x 1.4 Oil DIC M27 objective and a

746 CoolSnapHQ2 camera under the control of ZEN blue 3.3. Image analysis was performed using Fiji.

747 For direct fluorescent microscopy without prior staining, ~8 OD_{600} units were harvested, concentrated,

748 and fixed in 100 µl 4% PFA solution for 20 min at RT without shaking. Samples were than washed in

749 1x PBS and resuspended for imaging. Images were acquired on a Zeiss Axio Imager M2 equipped with

750 a 63x 1.4 Oil DIC M27 objective and a CoolSnapHQ2 camera under the control of ZEN blue 3.3, or on

751 a Leica Thunder Imager 3D cell culture microscope equipped with a HC PL APO 100x/1.44 Oil CORR

752 CS objective and a sCMOS camara (Leica DFC9000 GTC) under the control of LAS X (v 3.7.6)

753 software. Images acquired at the Leica microscope were processed with large volume computational

754 clearing (LVCC).

Isolation of mitochondria and spreading on EM grids

756 Crude mitochondrial fractions were isolated at a small scale as described previously [32,71]. Briefly, ~350

757 OD_{600} units were harvested, washed in water, and treated with 10 mM DTT in 100 mM Tris-SO$_4$ pH 9.4

758 for 20 min at 30°C. After washing in zymolyase buffer (1.2 M sorbitol, 20 mM KP_i pH 7.4), cells were

759 resuspended in 1.5 ml zymolyase buffer containing 10 mg 20T zymolyase (Seikagaku Biobusiness) and

760 incubated for 30 min at 30 °C. Spheroplasts were washed in zymolyase buffer and homogenized in

761 homogenization buffer [0.6 M sorbitol, 10 mM Tris/HCl pH 7.4, 1 mM ethylenediaminetetraacetic acid

762 (EDTA), 2 mM phenylmethylsulfonyl fluoride (PMSF), 0.2% (w/v) bovine serum albumin] by passing

763 the cell suspension 20 times through a 0.8 × 22 mm cannula. Cell debris and nuclei were removed by

764 centrifuging the suspension at 1,000 × g and crude mitochondria were isolated by centrifuging the

765 supernatant at 12,000 × g for 15 min. The mitochondrial pellet was resuspended in SEM buffer (250

766 mM sucrose, 1 mM EDTA, 10 mM MOPS/KOH pH 7.2) and the protein concentration was estimated

767 against an Albumin standard by the Bradford method. Aliquots were snap-frozen in liquid nitrogen and

768 stored at -80°C or directly used to apply on EM grids for plunge-freezing. For single-particle EM data

769 acquisition, purified mitochondria were splashed by hypo-osmotic swelling. Samples were spun down

770 at 20,000 × g for 10 min and pellets were resuspended in 10 mM MOPS pH 7.2. After 10 min on ice,

771 the mitochondria suspension was plunge-frozen on EM grids.

Preparation of spread yeast spheroplasts on EM grids

773 The preparation of spread yeast spheroplasts on EM grids was adapted from chromosome surface spread

774 protocols [27,28]. Briefly, ~3 OD_{600} units of cell culture were harvested, spun down for 2 min at 800 ×g,

775 resuspended in 200 µl of 1.2 M sorbitol in SPM and placed on ice. Cells were spheroplasted by adding

776 2 µl of 1 M DTT (30 °C, 15 min), followed by 5 µl 100T Zymolyase (1 mg/ml) (Seikagaku Biobusiness)

777 (30 °C, 15-30 min). From 8 min onwards, cells were regularly checked under the microscope to assess

778 the level of spheroplasting by mixing 1 µl of spheroplast suspension with 5 µl water on a glass slide.

779   Spheroplasted cells appear dark, whereas non-spheroplasted cells have a bright halo. When most of the

780   cell population is spheroplasted, 1 ml of ice-cold STOP solution (0.1 M MES, 1mM EDTA, 0.5 mM

781   MgCl$_2$, pH 6.4) was added. Spheroplasts were spun down at 800 × g for 2 min at 4 °C and carefully

782   resuspended in 100-200 µl ice cold STOP solution. 10 µl of spheroplast suspension was then mixed with

783   40 µl of 1% (v/v) Lipsol or 1% (v/v) NP-40 detergent immediately before adding them onto EM grids

784   for plunge-freezing.

785   **Plunge-freezing**

786   Meiotic yeast cells were cultured and plunge-frozen as described previously [25] with minor modifications.

787   Meiotic yeast cells were harvested and diluted to an OD$_{600}$ of 1-3 in SPM. Vegetatively growing cells in

788   YPD were harvested at an OD$_{600}$ of ~0.8 and concentrated in SPM to OD$_{600}$ of 1-3 by spinning for 2 min

789   at 650 × g. Yeast cells were kept on ice until they were plunge-frozen with a Vitrobot Mark IV (Thermo

790   Fisher Scientific) [72]. 4 µl of cell suspension was applied onto the negatively glow-discharged EM grids

791   (R2/2 Cu 200 mesh, specially treated, Quantifoil). Using a Teflon sheet on one side, grids were back-

792   blotted either once for 5-6 s or twice for 3-5 s at 4 °C, 95% humidity, before plunging into the liquid

793   ethane-propane mixture [37% (v/v) ethane] [73]. Intact and splashed mitochondria were prepared as

794   described above. Samples were mixed with 10 nm BSA-coated colloidal gold particles

795   (Cytodiagnostics) in a ratio of 5:1 and then 3 µl of sample was applied onto negatively glow-discharged

796   EM grids (R2/2 or R2/1 Cu 200 mesh, specially treated, Quantifoil). Grids were back-blotted for 4-5 sec

797   at 4 °C, 95% humidity and were plunge-frozen. Spread yeast spheroplasts were prepared as described

798   above. The spheroplast Lipsol mixture was mixed with gold particles in a 10:1 ratio and then 3 µl of

799   sample was applied onto the negatively glow-discharged EM grids (R2/1 Cu 200 mesh, specially treated,

800   Quantifoil). Grids were back-blotted for 4-5 sec at 4 °C, 95% humidity and were plunge-frozen.

801   **Cryo-focused ion beam milling**

802   Due to the thickness of frozen-hydrated yeast cells, plunge-frozen cells were cryo-focused ion beam

803   (FIB) milled with a Crossbeam 550 FIB-SEM instrument (Carl Zeiss Microscopy) before cryoET

804   imaging as described previously [25]. The FIB-SEM instrument was equipped with an SE2 detector (Carl

805   Zeiss Microscopy), an in-lens secondary electron detector (Carl Zeiss Microscopy), a copper band-

806   cooled mechanical cryo-stage (Carl Zeiss Microscopy), and an integrated VCT500 vacuum transfer

807   system (Leica Microsystems). In brief, plunge-frozen EM grids were clipped into FIB milling Autogrids

808   (Thermo Fisher Scientific) and mounted onto a pre-tilted cryo-FIB Autogrid holder (Medeiros et al.,

809   2018) (Leica Microsystems) using a VCM loading station (Leica Microsystems). Using the VCT500

810   shuttle, the Autogrid holder was transferred to an ACE600 (Leica Microsystems) to cryo-sputter-coat

811   the sample with a 4 nm thick layer of tungsten. Afterwards, the samples were loaded into the Crossbeam

812   550 using the VCT500 vacuum transfer system. Inside the FIB-SEM, grids were additionally coated

813 with organoplatinum. Targets were selected with the SEM and automated sequential FIB milling was
814 set up. A pattern with four currents was used (rough milling: 700 pA, 300 pA, and 100 pA; polishing:
815 50 pA) for milling, targeting for a ~300 nm thick lamella. After milling, the Autogrid holder was
816 transferred back to the VCM loading station with the VCT500 shuttle and grids were unloaded and
817 stored in liquid nitrogen until cryoET imaging.

818 **CryoLM**

819 Plunge-frozen EM grids were imaged with a Zeiss LSM900 equipped with Airyscan2 detector and a
820 Linkam CMS196V3 cryo-stage in a de-humidified room. EM grid overviews were collected with a
821 5x/0.2 DIC C Epiplan-Apochromat objective to localize the regions of interest. Afterwards, z-stacks
822 were collected with a 100x/0.75 DIC LD EC Epiplan-Neofluar (WD = 4 mm) objective. Confocal
823 imaging tracks were used to visualize Acs1-GFP signal as well as the EM grid with transmitted and
824 reflective light. Confocal imaging stacks were deconvolved with Zeiss LSM Plus processing and
825 maximum intensity projections were generated in ZEN Blue (Carl Zeiss Microscopy, v.3.5) software.

826 CryoLM data was then used to correlate targets for cryoET data collection in x-y dimensions (described
827 below) [74]. For that, cryo-LM images were imported into SerialEM [75] and aligned to the corresponding
828 EM overviews based on prominent landmarks. To visualize correlated cryoLM and cryoEM images after
829 data collection, low-magnification EM overviews were low-pass filtered using 'mtffilter' and converted
830 to tiff files using 'mrc2tif' in IMOD package [76]. These images together with the cryoLM data were
831 imported in ZEN Connect (within ZEN Blue, Carl Zeiss Microscopy, v.3.5) for correlation with the
832 Point Alignment Wizard.

833 **CryoET data collection, reconstruction, and segmentation**

834 CryoET datasets were collected on Titan Krios transmission electron microscopes (TEM) (Thermo
835 Fisher Scientific) operating at 300 kV and equipped with Quantum LS filter and K2 Summit direct
836 electron detectors (Gatan) (Krios1), equipped with Quantum LS filter and K3 direct electron detectors
837 (Gatan) (Krios2), and BioContinuum imaging filter and K3 direct electron detectors (Gatan) (Krios3).
838 Low magnification overviews were recorded for navigation and targets were selected for the subsequent
839 tilt series collection using SerialEM [75].

840 For lamellae, tilt series collections were performed using a bidirectional scheme with an angular range
841 between ±70° to ±50°, depending on the pre-tilted geometry of lamella, with 2° increment at a defocus
842 of -8 μm. The pixel sizes in different datasets were 4.34 Å (Krios1) or 4.51 Å (Krios3) or 4.57 Å (Krios2)
843 at the specimen levels. The accumulated dose per tilt series is ~120 e$^-$/Å^2. For purified mitochondria, tilt
844 series collections were performed using a dose-symmetric scheme with an angular range between +60°
845 to -60° with 2° increment at a defocus of -8 μm. The pixel size was 2.75 Å (Krios1) or 2.68 Å (Krios3)

846 at the specimen level and the total dose per tilt series is ~160 e⁻/Å^2. For spread yeast spheroplasts, the

847 same collection scheme was used as for purified mitochondria and the pixel sizes at the specimen level

848 were the same as for the lamella. The total dose per tilt series is ~130 e⁻/Å^2.

849 Frames were aligned using 'alignframes' and tomograms were reconstructed using the IMOD package

850 [76]. Tomograms shown in the figures were binned at the level of 4 and the contrasts were improved using

851 the deconvolution filter 'tom_deconv' [77].

852 AI-based segmentations were generated in Dragonfly software (Object Research Systems, v. 2022.2) as

853 described previously [78]. Briefly, filtered tomograms were loaded into Dragonfly and further processed

854 by histogram equalization, Gaussian and Unsharp filtering. Afterwards, a U-Net (with 2.5D input of 5

855 slices) was trained to recognize background voxels, filaments, and membranes within the tomograms.

856 All AI-segmentations were manually cleaned up in Dragonfly, exported as binary tiff files and converted

857 to mrc files using 'tif2mrc' in IMOD. Segmentations were visualized in UCSF ChimeraX [79].

858 **Sub-tomogram averaging**

859 Sub-tomogram averaging of filaments from different datasets was performed in Dynamo software [80].

860 The individual filaments were manually picked from reconstructed tomograms at a binning factor of 4

861 using the 'filamentWithTorsion' model in Dynamo. The different filaments were segmented with the

862 corresponding inter-segment distance (8.8 nm for Ald4 dataset, 5.5 nm for Acs1 dataset) before particle

863 cropping. The cropped sub-volumes from each dataset (Ald4 filaments in the isolated mitochondria: 564

864 particles from 3 tomograms; Acs1 filaments in the spread yeast spheroplasts: 452 particles from 3

865 tomograms) were assigned random azimuth orientations using 'dynamp_table_randomize_azimuth' and

866 were firstly subjected to the averaging without imposing symmetry. The symmetry information of

867 individual filaments was then deduced from the asymmetric reconstruction and was applied in the

868 downstream averaging analyses. All particles were subjected to one round of coarse alignment with

869 rough angular search steps, and the particles were then split into half-datasets based on the odd-and-

870 even order with 'dteo' package in Dynamo. Each half-dataset was subjected to fine alignment with

871 precise angular search steps against the same reference. The Acs1 dataset was analyzed using fine

872 alignment at the binning factor of 2, while the Ald4 dataset was analyzed at the binning factor of 4. The

873 final averaged volumes from individual half-datasets were used to estimate the resolution based on the

874 Fourier shell correlation (FSC) [81] using 'relion_postprocess' [82]. The final resolution of averaged maps

875 of Ald4 filaments from intact mitochondria was 44 Å, whereas the resolution of Acs1 filaments from

876 spread yeast spheroplasts was 18.3 Å.

CryoEM single-particle data collection

CryoEM data collection parameters are summarized in Table S1. CryoEM datasets of Ald4 filaments from spread yeast mitochondria were collected at a nominal magnification of 81,000 × (an effective pixel size of 0.55 Å at super-resolution) using the SerialEM program on Krios2. Low magnification overviews were recorded for navigation purposes to target filaments and the data was collected as movie stack in super-resolution mode, with the 2.5 s total exposure time at a defocus value from -1.2 to -2.8 μm. Each stack contains 50 frames, and the accumulated electron dose was ~60 e⁻/Å². The frames of the stack were aligned and applied with dose weighting at the binning factor of 2 using 'MotionCor2' [83] (an effective pixel size of 1.1 Å). The CTF parameters of micrographs were estimated using 'Gctf' [84]. A total of 531 micrographs in two batches were collected for image processing.

CryoEM datasets of Acs1 filaments from spread yeast spheroplasts were collected at a nominal magnification of 130,000 × (an effective pixel size of 0.535 Å at super-resolution) using the SerialEM program on Krios1. The data collection strategy was performed same as above. The data was collected as movie stack in super-resolution mode, with the 8 s total exposure time. Each stack contains 32 frames and the accumulated electron dose was ~60 e⁻/Å². The motion correction and CTF parameter estimation were performed the same as above (an effective pixel size of 1.07 Å). A total of 1,084 micrographs were collected for image processing.

CryoEM image processing, identification of Ald4, and structural modeling

To determine the structure of the filament observed in the mitochondria, 132 micrographs in the first batch of dataset were used to generate an initial model (Figure S3A). Briefly, the filaments were manually picked using Relion 3.0 [85] and 22,365 segments were extracted with an inter-box distance of 42 Å. One round of 2D classification at the binning factor of 4 was performed to remove bad particles, and the particles in good classes were then subjected to 3D refinement without imposing helical parameter but with 2-fold symmetry that was deduced from the sub-tomogram averaged volume. The initial helical parameters were interpreted from the reconstructed map using 'relion_helix_toolbox' [86] and were then applied and locally refined in the following helical reconstruction [86]. The bad particles were further removed by one round of 2D classification without sampling after helical reconstruction and the following 2D classification. A total of 11,863 particles were used to reconstruct ~6.8 Å resolution of filament structure at the binning factor of 2, which was imposed a 2-fold symmetry and helical parameters (twist = 96.2˚, rise = 42.2 Å).

To identify the components in the filament assembly, the molecular weight of the sought-after protein was firstly estimated to be ~30-70 kDa based on the volume size of one filament subunit. To shortlist potential candidates, we cross-compared mass spectrometry (MS) data of mitochondrial matrix/inner membrane proteins [32] and MS data covering protein expression profiles in meiosis [31] (Table S3).

911   Providing this list to structural docking of Alphafold [29,30] predicted candidate protein structures showed

912   that the Ald4 protein fits the map.

913   To further verify the protein identity, we continued image processing using 531 micrographs collected

914   in two batches. Since Ald4 homolog protein was reported to form a tetramer in solution and crystal

915   structure (Aldh2, PDB entry: 1NZZ) [33], there were still two symmetry possibilities for the filament

916   assembly: proteins form a dimer (C2 symmetry) or tetramer (D2 symmetry) and then assemble into the

917   filament. The different symmetry possibilities would request different inter-box distance for filament

918   segmentations.

919   To investigate this, we first assumed C2 symmetry and segmented the filaments with an inter-box

920   distance of 42.2 Å. The extracted segments were subjected to 2 rounds of 2D classifications at the

921   binning factor of 4 and 2, and the particles in good classes were used for helical reconstruction at the

922   binning factor of 1, where the helical parameters (twist = 96.2°, rise = 42.2 Å) were applied and

923   optimized during refinement. A final 4.2 Å resolution filament structure was determined, however, the

924   densities around the secondary structure (e.g., α helices) were unreasonable, suggesting that a wrong

925   symmetry was applied. Thus, we switched to D2 symmetry in the following image processing. The

926   filaments were segmented with an inter-box distance of 84.4 Å and were extracted with a larger box size

927   (320 pixels). The particles were subjected to a round of 2D classification at the binning factor of 4 and

928   the particles in good classes were used for the helical reconstruction at the binning factor of 1. A filament

929   structure with 6.6 Å resolution was determined, assuming C2 and helical symmetry (twist = 96.2°, rise

930   = 84.6 Å). Moreover, 2D classification analysis revealed that tetramers adopt two different types of

931   stacking for the filament assembly: helical and non-helical (Figure S3B). To further improve the

932   resolution, the central tetramer in each segment was centered and re-extracted using a smaller box size

933   (200 pixels) (Figure S3A). The particles with smaller box sizes were than subjected to 3D refinement

934   followed by local 3D classification. The particles in good 3D classes were combined and were subjected

935   to the next round of 3D refinement imposed C2 and local symmetry (D2). One round of CTF parameter

936   optimization and particle polishing were further applied to improve the map quality. A final resolution

937   of 3.8 Å structure was determined from 29,307 particles assuming C2 and local symmetry (together in

938   D2 symmetry). The map quality was further improved using 'deepEMhancer' [87]. The local resolution

939   was estimated using Relion (Figure S3C).

940   The structure was manually refined in COOT [88], the models were further refined in real-space using

941   iterative refinements of RosettaCM [89] and 'phenix.real_space_refine' [90]. The refined model was

942   evaluated using 'phenix.molprobity' [90] and the model vs. map FSC was calculated using

943   'phenix.mtrifage' [90] (Figure S3D-E). In the final atomic model of an Ald4 filament subunit, 24 residues

944   of the N-terminus were missing due to invisible densities. The bound NAD molecule was included in

945   the final model (Table S1).

946   The surface contact sites between Ald4 tetramers were firstly analyzed by PDBePISA ['Protein
947   interfaces, surfaces and assemblies' service PISA at the European Bioinformatics Institute.
948   (http://www.ebi.ac.uk/pdbe/prot_int/pistart.html), [91]] and were then manually checked in COOT.

**CryoEM image processing, identification of Acs1, and structural modeling**

950   To generate the initial filament model and estimate the helical parameters, micrographs of 0˚ tilt in the
951   datasets of spread yeast spheroplasts were used for the processing (Figure S6A). The filaments were
952   picked manually with the start-end coordinate pairs using Relion 3.0. The filaments were segmented
953   with an inter-box distance of 60 Å and were then subjected to 2 rounds of 2D classifications. The
954   particles in the good classes were selected for 3D auto-refinement using helical reconstruction without
955   imposing helical symmetry but with 3-fold symmetry that was deduced from sub-tomogram averaged
956   volume. The helical parameters were estimated from the initial reconstruction in real space using
957   'relion_helix_toolbox' and were optimized for the second round of 3D auto-refinement at the binning
958   factor of 4. The refined helical parameters were: twist = 13.58˚, rise = 54.62 Å.
959   To determine the high-resolution filament structure, 1,084 micrographs were collected as mentioned
960   above and used for the imaging processing. The filaments were manually picked and 108,349 segments
961   were extracted with an inter-box distance of 55 Å. Bad particles were removed through 2 rounds of 2D
962   classifications at the binning factors of 4 and 2 (Figure S6B). The particles in good classes were then
963   applied to the helical reconstruction at the binning factor of 2, where the helical parameters from the
964   reconstruction of 0˚ tilt were applied and locally refined in the follow-up processing steps. One round
965   of 2D classification without sampling was performed after helical reconstruction to remove the mis-
966   aligned particles. The remaining particles were subjected to the 3D helical reconstruction at the binning
967   factor of 1 and a subsequent round of 2D and 3D classifications without sampling. The particles from
968   good classes were then subjected to another round of 3D classification and only one 3D class (class IV
969   in Figure S6B) was used for the helical reconstruction. One round of CTF parameters optimization and
970   particle polishing were further performed to improve the map quality. The final 3.5 Å resolution filament
971   structure was determined from 17,169 particles imposing 3-fold symmetry and helical parameters (twist
972   = 13.03˚, rise = 53.61 Å) (Figure S6B). The map quality was further improved using 'deepEMhancer'.
973   The local resolution was estimated using Relion (Figure S6C).
974   To identify the components in the filament assembly, the Cα backbone of one filament subunit was
975   manually traced in COOT and was then subjected to DALI search
976   (http://ekhidna2.biocenter.helsinki.fi/dali/) [35], which revealed the Acs1 protein as a potential candidate.
977   The crystal structure of Acs1 protein (PDB entry: 1RY2) [36] was then docked into the map and manually
978   refined using COOT and then subjected to the same refinements and structural validation as mentioned
979   above for Ald4 (Figure S6D-E). In the final atomic model of Acs1 filament subunit, 37 residues in the

980   N-terminus were missing due to invisible densities. The intermediary product acetyl-AMP was included

981   in the final model (Table S1).

982

SUPPLEMENTARY FIGURES
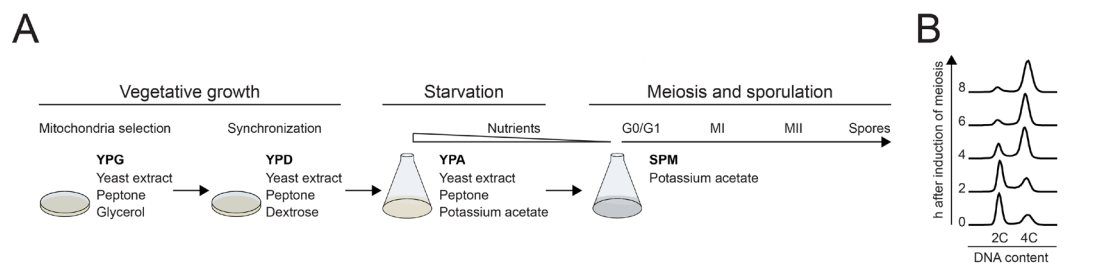
Figure S1. Meiotic time course.

(**A**) Schematic representation of the experimental setup to perform a meiotic time course. Vegetatively growing diploid *S. cerevisiae* cells were plated for single colonies on YPG plates to select for strong respiratory growth. Single colonies were then expanded before they were starved in YPA medium containing the non-fermentable carbon source potassium acetate. Arrested cells at G0/G1 were transferred to sporulation medium (SPM) lacking the nitrogen source in order to induce the meiotic cell division program (Pre-meiotic G0/G1, first meiotic division MI; second meiotic division MII, and spore formation).

(**B**) FACS analysis of the DNA content to monitor meiotic progression. DNA content of meiotic cell cultures was analyzed by FACS at regular time intervals after the induction of meiosis (transfer of cells to SPM). Note that most of the cells duplicated their genomes after ~4 h in SPM. Shown is a representative time course.

998
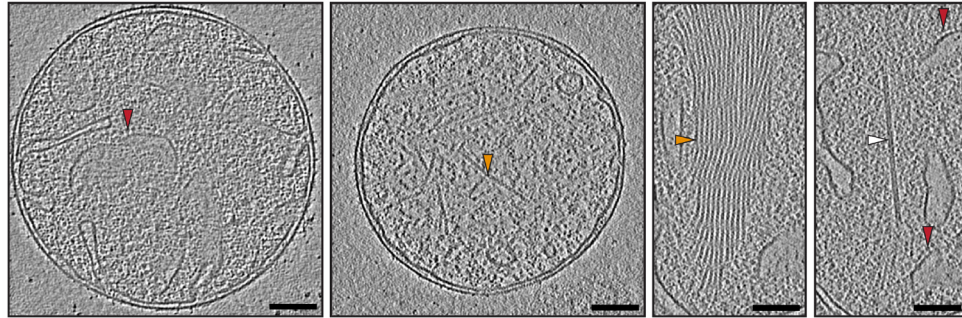
Figure S2. CryoET of purified meiotic mitochondria.

Visualization of the ultrastructure of purified mitochondria. Shown are example slices through cryo-tomograms of purified mitochondria from meiotic cell cultures collected between 6-8 h after induction of meiosis. Red arrowheads point to putative F_OF_1-ATP synthases on cristae. Orange arrowheads show single filaments and arrays as seen in Figure 3A, whereas the white arrowhead points to a different type of filament within purified mitochondria. Shown are projections of 5.5 nm thick slices. Scale bars: 100 nm.

1007

42
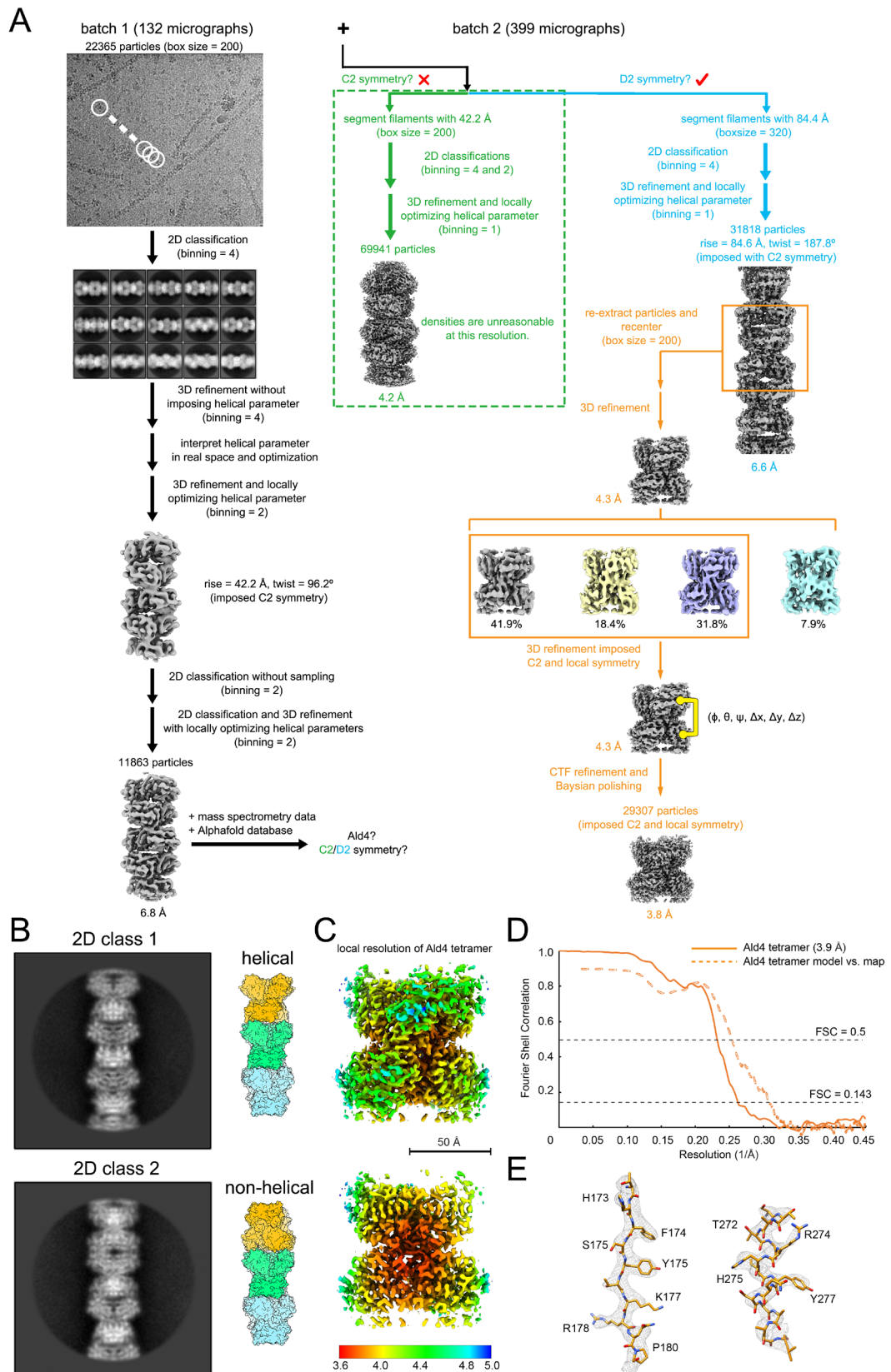
Figure S3. Flowchart of processing cryoEM data for Ald4 filaments.

**(A)** Flowchart for the cryoEM reconstruction of the Ald4 filament. See METHODS and Supplementary Table S1 for details.

(B) Representative 2D classes and the corresponding schematics showing that Ald4 tetramers follow two different stacking manners for the filament assembly: helical (top) and non-helical (bottom). Individual tetramers are colored in orange, green, and blue respectively.

(C) Local resolution (indicated by colors in Å) maps of the Ald4 tetramer. Scale bar: 50 Å.

(D) Plots showing the gold standard FSC curve of the cryoEM reconstruction of the Ald4 tetramer (orange) and the corresponding model *vs.* map FSC curve (dashed orange).

(E) Stick and density mesh diagrams showing representative density maps of the Ald4 tetramer. Stick models and density meshes are colored orange and gray respectively.
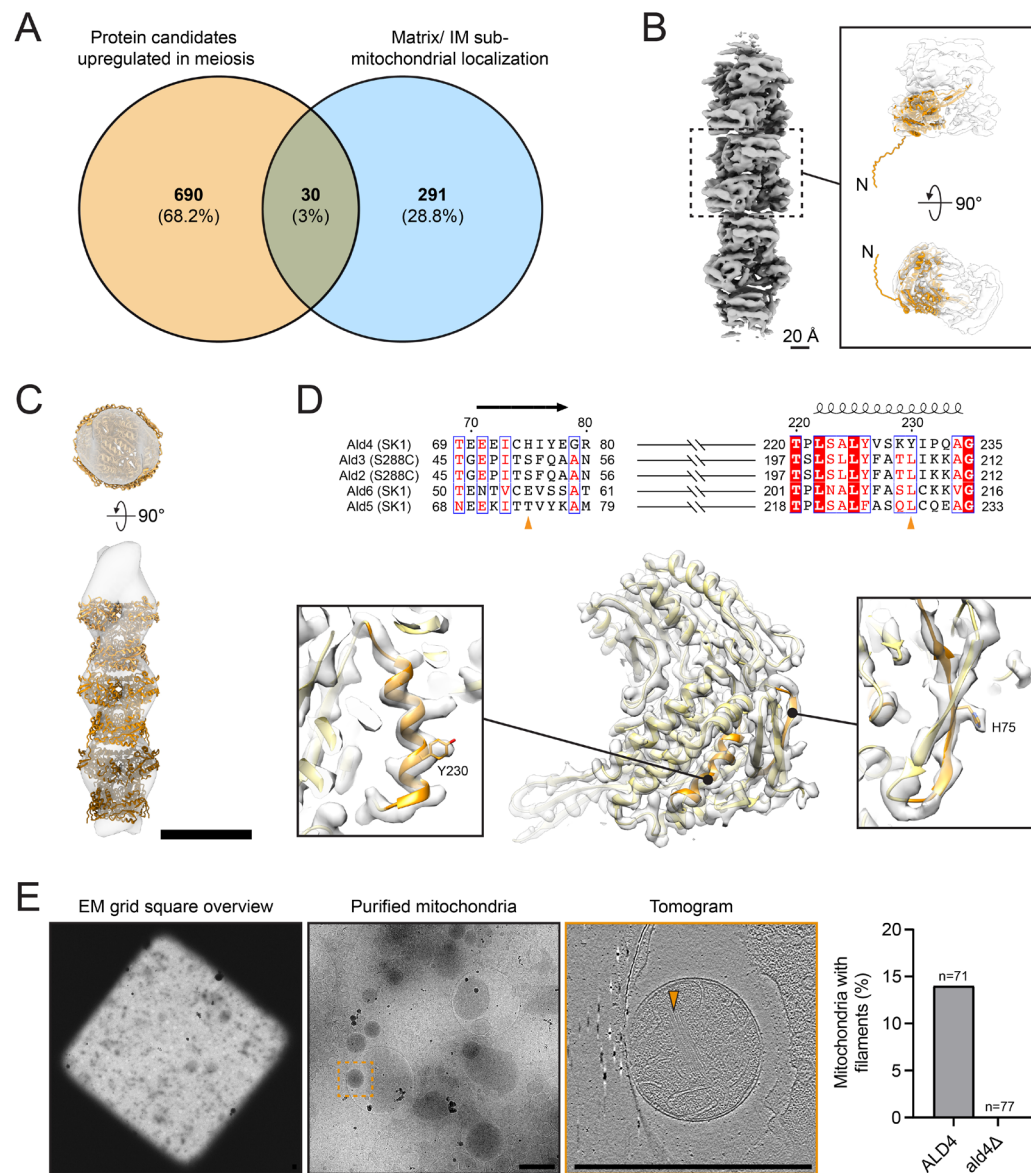
1020

Figure S4. Validation of Ald4 protein identity.

**(A)** Comparing data obtained from two independent mass spectrometry analyses yields 30 candidate proteins forming the mitochondrial filaments. Shown is a Venn diagram with proteins upregulated in meiosis [31] colored orange together with high confidence mitochondria proteins, which localize to the mitochondrial matrix or inner membrane (IM) colored blue [32]. Percentage of total input is indicated in each bin.

(B) Ribbon and shadowed surface diagrams showing that Ald4 is a potential candidate from **(A)** forming the mitochondrial filaments. Left: the helical reconstructed map of the mitochondrial filament. One helical repeat is highlighted with a dashed black box. Right: docking of the predicted Ald4 structure from Alphafold [29,30] (orange) into one subunit of one helical repeat.

44

1031 **(C)** Docking of the high-resolution structure of three Ald4 tetramers with the sub-tomogram averaged
1032 volume of Ald4 filaments from splashed mitochondria. Three layers of Ald4 tetramers are shown as
1033 ribbons and are colored in different shades of orange as in Figure 4D, while the averaged volume (also
1034 shown in Figure 3B) is transparent and colored gray. Scale bar: 10 nm.

1035 (**D**) Reconstructed map unambiguously identifies Ald4 as the only filament component. Top: sequence
1036 alignments of different Ald isoforms (Ald4-6 from SK1 strain, Ald2-3 from S288C strain). Identical
1037 residues are shown in white on a red background, while similar residues are shown in red. The blue
1038 boxes indicate the conserved positions. The secondary structure of Ald4 is shown above the
1039 corresponding sequences. The image is made using Espript [92]. Two distinguishing residues of Ald4 (H75
1040 and Y230) are highlighted by orange arrowheads and are shown in the bottom panel. Bottom: ribbon
1041 and shadowed surface diagrams showing the fitting of the Ald4 model with the reconstructed map. The
1042 density map is colored gray and is shown transparent, while the overall model is colored yellow. The
1043 aligned parts shown on the top panel are colored orange, while zoom-ins show the densities of two
1044 distinguishing residues (H75 and Y230).

1045 **(E)** Mitochondrial filament arrays consist of Ald4. Left to right: to check for the presence of filaments,
1046 purified mitochondria from meiotic cell cultures are picked in the EM grid square overview followed by
1047 cryoET imaging. The corresponding 5.5 nm thick slice of the cryo-tomogram shows an example
1048 mitochondrion containing filaments. Scale bars: 1 μm. Right: shown are percentages of meiotic
1049 mitochondria (6 h after induction of meiosis) containing filaments and the total number of mitochondria
1050 (n) analyzed for each genotype are indicated.
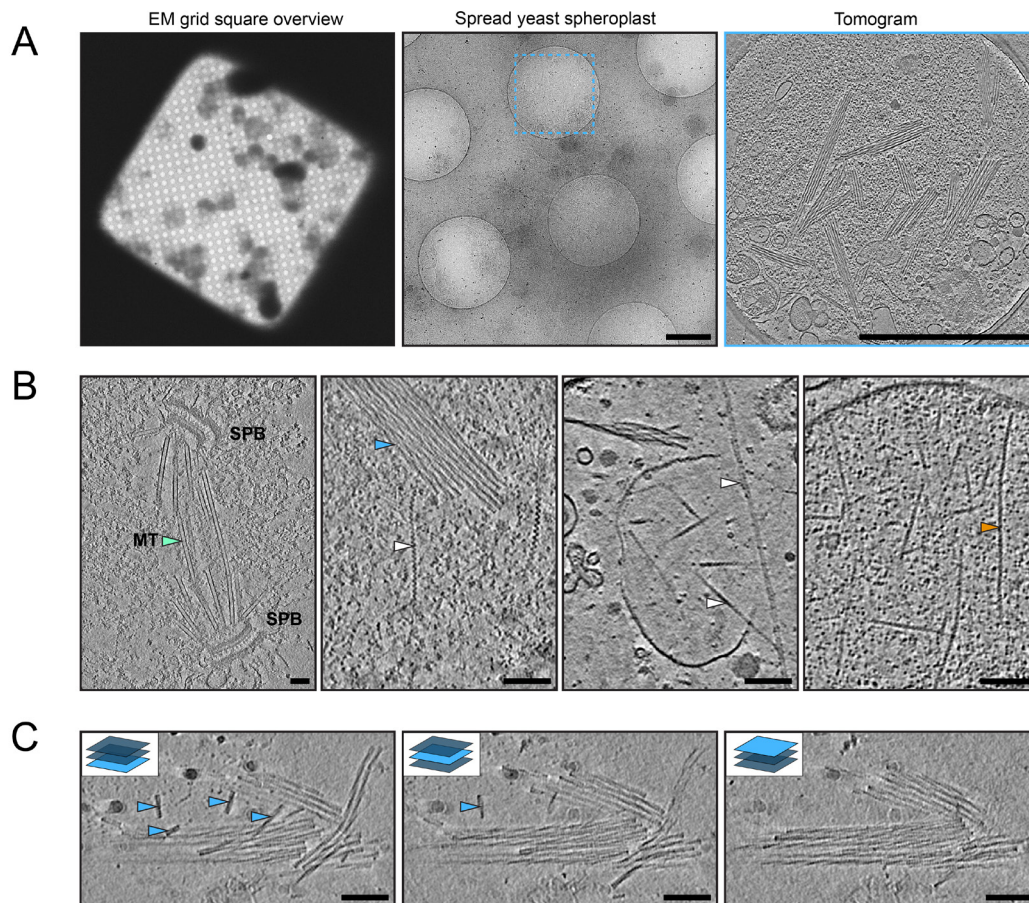
1051

Figure S5. CryoET on spread spheroplasts.

(A) Spread yeast spheroplasts allow for direct cryoET imaging. Left: overview of an example EM grid square with spheroplasts. Middle: cryoEM micrograph of an example spread spheroplast from a *ndt80Δ* strain arrested in prophase I, 8 h post induction of meiosis. Right: slice through the cryo-tomogram collected on parts of the spread indicated by the blue box. Note that straight filament assemblies in different directions can be observed as shown in Figure 4A. Shown is a projection of 9.14 nm thick slices. Scale bars: 1 μm.

(B) Spread yeast spheroplasts enable the visualization of various macromolecular assemblies. Shown are example slices through cryo-tomograms of spreads from meiotic cell cultures. Green arrowhead points to microtubules (MT) branching from spindle pole bodies (SPB). Blue arrowhead shows filament bundles, orange arrowhead shows single filaments in spread mitochondria, white arrowheads point to other types of filaments. Shown are projections of either 8.68 nm or 9.14 nm thick slices. Scale bars: 100 nm.

(**C**) Slice through cryo-tomogram of potential filament bundle (dis-)assembly intermediates. Note that short single filaments point towards a bundle containing multiple long filaments. Short filaments are

1067   highlighted with blue arrowheads. Shown are projections of 9.14 nm thick slices at different z-heights

1068   of the tomogram, which are 7.31 nm apart. Scale bar: 100 nm.

1069
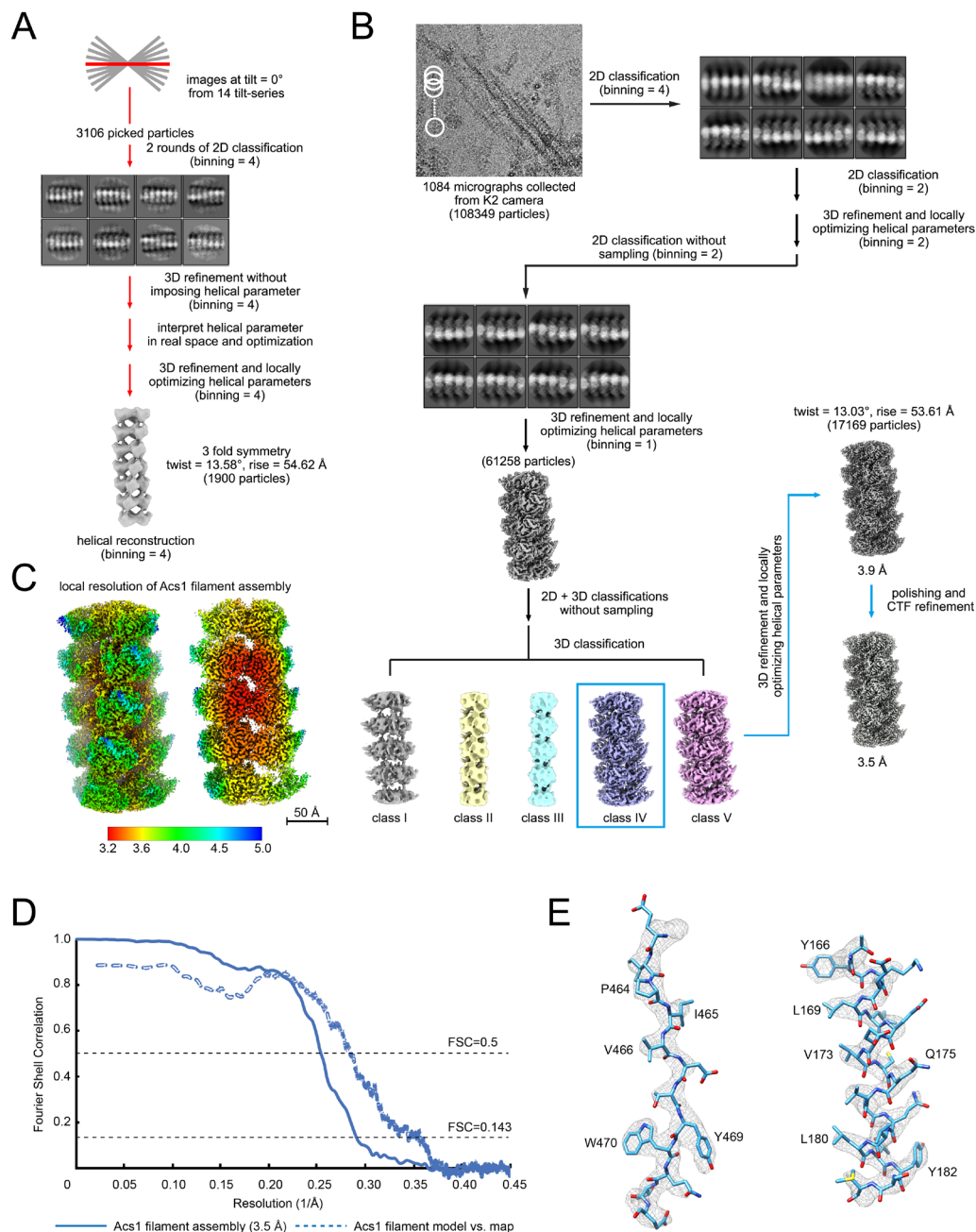
1070

Figure S6. Flowchart of processing cryoEM data for Acs1 filaments.

(A) Flowchart to generate the initial filament model and to determine the initial helical parameters using individual images (tilt = 0°) from different tilt series. See METHODS for details.

(B) Flowchart for the cryoEM reconstruction of Acs1 filament. See METHODS and Supplementary Table S1 for details.

(C) Local resolution (indicated by colors in Å) maps of the Acs1 filament structure. Scale bar: 50 Å.

(D) Plots showing the gold standard Fourier Shell Correlation (FSC) curve of the cryoEM reconstruction of Acs1 filament (blue) and the corresponding model *vs.* map FSC curve (dashed blue).

1079   **(E)** Stick and density mesh diagrams showing the representative density maps of the Acs1 filament

1080   structure. Stick models and density meshes are colored blue and gray respectively.

1081
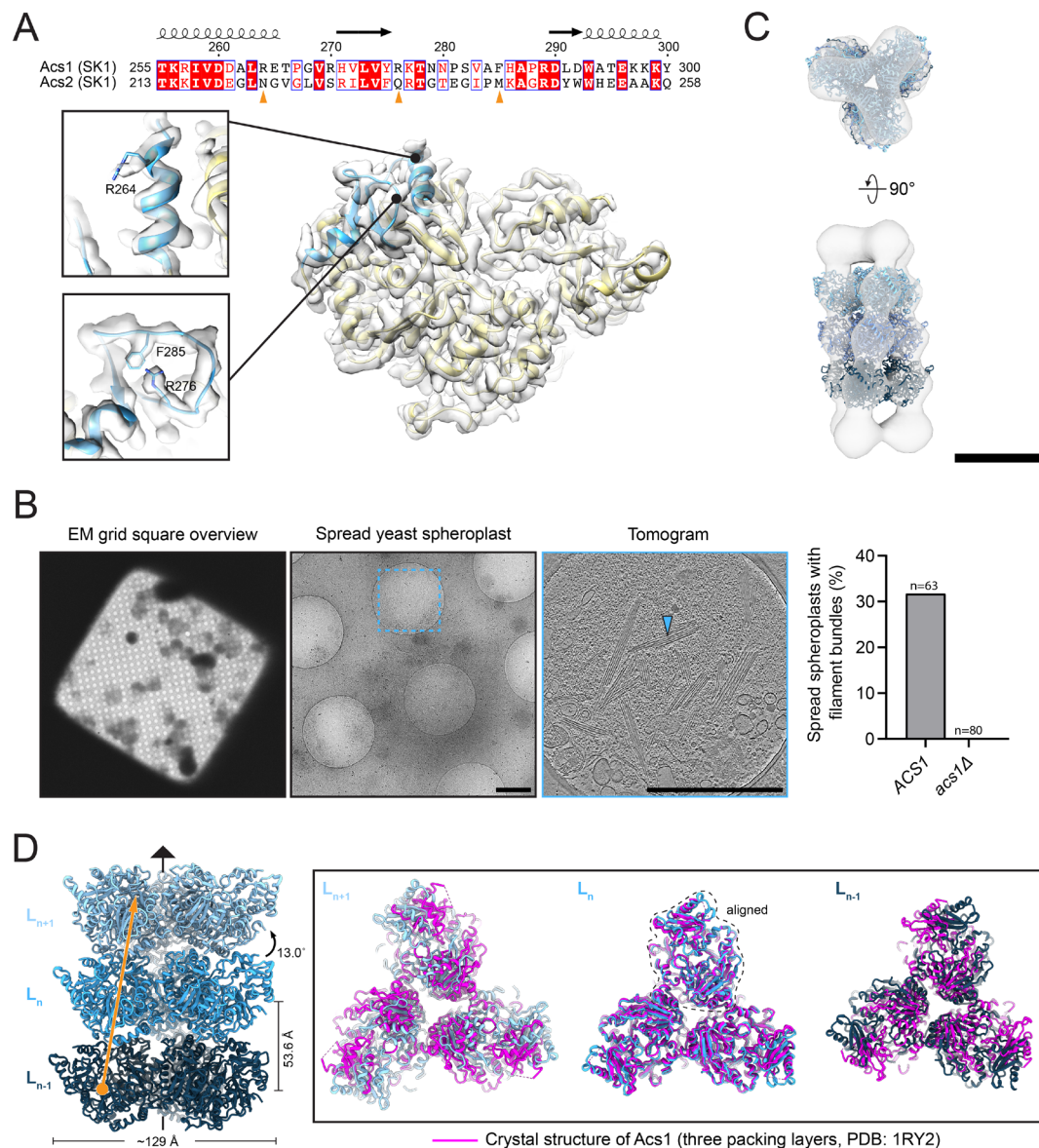
Figure S7. Validation of Acs1 protein identity.

(A) Reconstructed map unambiguously identifies the Acs1 trimer as the only filament component. Top: sequence alignments of Acs1 and its isoform Acs2 from the SK1 strain. The identical residues, similar residues, and the conserved positions are shown in the same style as in Figure S4D. The secondary structure of Acs1 is shown above the corresponding sequences. Three distinguishing residues of Acs1 (R264, R276, and F285) are highlighted by orange arrowheads and are shown on the bottom panel. Bottom: ribbon and shadowed surface diagrams showing the fitting of Acs1 model with the reconstructed map. The density map is colored gray and is shown in transparent, while the overall model is colored yellow. The aligned parts shown on the top panel are colored blue, while zoom-ins show the densities of three distinguishing residues (R264, R276, and F285).

50

1093   **(B)** Filament bundles consist of Acs1. Left to right: to check for the presence of filament bundles, spread

1094   spheroplasts are picked in the EM grid square overview. Afterwards, cryoEM micrographs or

1095   tomograms, if needed, are collected to assess whether filament bundles are present (highlighted with a

1096   blue arrowhead). Scale bars: 1 μm. Shown are the same images as in Figure S5A. Right: shown are

1097   percentages of meiotic spread spheroplasts (6 h after induction of meiosis) containing filament bundles

1098   and the total number of spreads (n) analyzed for each genotype are indicated.

1099   **(C)** Docking of the high-resolution structure of Acs1 filament fits the sub-tomogram averaged volume

1100   of Acs1 filaments from spread yeast spheroplasts as shown in Figure 4B. Three layers of Acs1 trimers

1101   are shown in ribbon and colored in different shades of blue as in Figure 4D, while the averaged volume

1102   is transparent and colored gray. Scale bar: 10 nm.

1103   **(D)** Structural superimposition of Acs1 in the filament assembly and the crystal packing (PDD entry:

1104   1RY2) [36]. Left: Ribbon diagrams showing three layers of Acs1 trimers, which are colored in different

1105   shades of blue as in Figure 4D. The helical parameters (twist = 13.0˚, rise = 53.6 Å) are labeled and a

1106   single strand is marked with an orange arrowhead. The 3-fold axis is represented by a triangle. Right:

1107   Magnified top view of three individual consecutive layers in the Acs1 filament aligned with the crystal

1108   packing of yeast Acs1 based on the structural superimposition of the central layer (L_n). Note that the

1109   central layer is nicely aligned, while the neighboring layers (L_{n+1}, L_{n-1}) mismatch due to the helical twist

1110   in the Acs1 filament.

1111
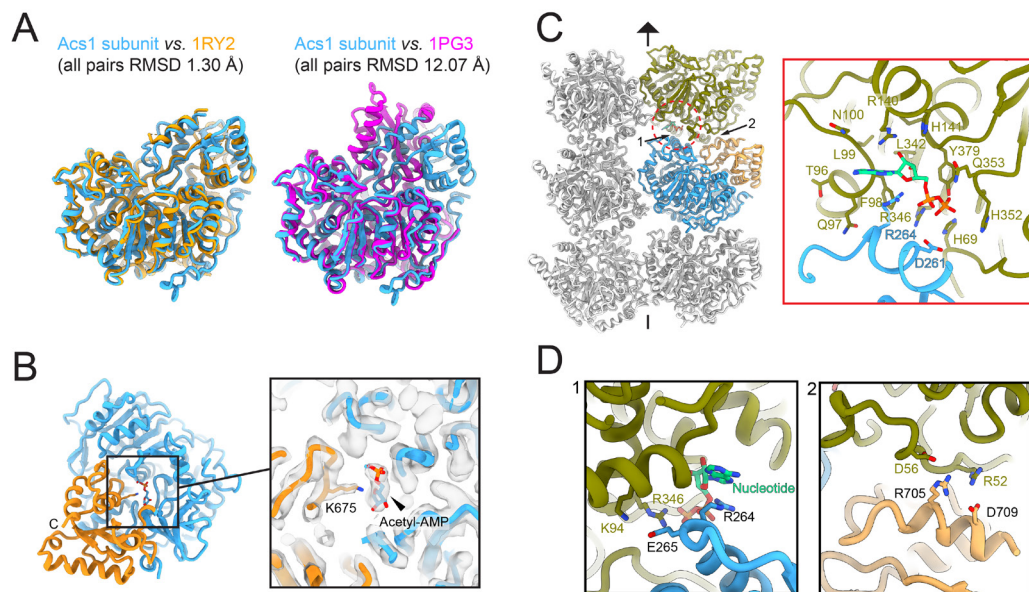
Figure S8. Acs1 subunits bind to two metabolites to form the filament.

**(A)** Ribbon diagrams showing that the Acs1 subunit in the filament conformation fits the state that accomplishes the first step of the enzymatic reaction. Structural superpositions show the structural difference between Acs1 subunit from the filament conformation (blue) with the yeast Acs1 binary complex (PDB entry: 1RY2 [36], orange, left) representing the first step of the enzymatic reaction, compared to the bacterial ACS homolog ternary complex (PDB entry: 1PG3 [40], magenta, right) representing the second step of the enzymatic reaction.

(B) Ribbon and stick diagrams showing that the acetyl-AMP intermediate interacts with the catalytic residue K675 of Acs1. The Acs1 structure is shown ribbon style and is color-coded as in Figure 5C, whereas the acetyl-AMP intermediate is shown in stick style. The C-terminus of Acs1 is labeled. Zoom-in on the catalytic site is shown on the right, highlighting the contact between the catalytic key residue K675 and the acetyl-AMP intermediate. The density of Acs1 subunit is colored gray and is shown in transparent, while the side chain of K675 is shown in stick style.

(C) Ribbon and stick diagrams showing the metabolic nucleotide (potentially ADP) bound to two consecutive Acs1 trimer layers. Three Acs1 trimer layers are color-coded as in Figure 5C and the 3-fold axis is represented by a triangle. The binding site of the metabolic nucleotide is highlighted with a red dashed circle and the zoom-in is shown to the right. The metabolic nucleotide and the side chains of the contacting residues are labeled and are shown in stick style. Two interfaces between adjacent Acs1 subunits are marked (1 and 2) and the details are shown in panel (**D**).

(D) Ribbon and stick diagrams showing that salt bridge pairs contribute to the Acs1 filament assembly. Zoom-ins show the corresponding interfaces highlighted in panel (**C**). The metabolic nucleotide

52

1134   (potentially ADP) and the side chains of residues participating in salt bridge pairs are labeled and are

1135   shown in stick style.

1136

Spores 10h after induction of meiosis

Acs1-GFP (MIP LVCC)

Brightfield
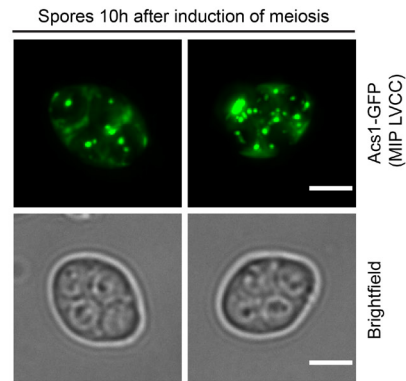
1137

1138 **Figure S9. Acs1 C-terminally tagged with GFP forms foci in ascospores.**

1139 Cells expressing Acs1-GFP from the endogenous promotor were sporulated and imaged by fluorescent

1140 light microscopy. Shown are two representative images of maximum intensity z-projections (MIP) after

1141 large volume computational clearing (LVCC) and the corresponding Brightfield image of the

1142 ascospores. Scale bar: 3 μm.

1143
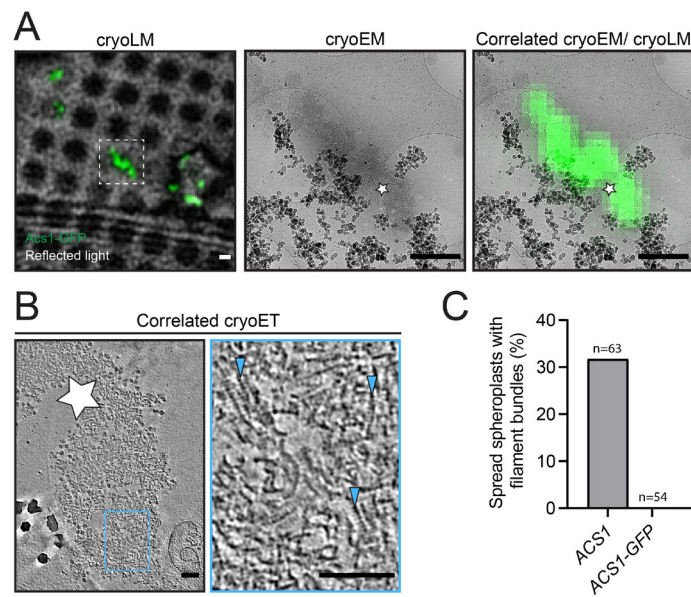
Figure S10. Acs1 C-terminally tagged with GFP forms short single filament aggregates but not elaborate bundles.

(A) Correlation of Acs1-GFP signal in cryo-confocal light microscopy (cryoLM) with cryoEM. Left: cryoLM of a Acs1-GFP rod from a meiotic spread yeast spheroplast (6 h after induction of meiosis) on an EM grid. Shown is an overlay of maximum intensity projections of Acs1-GFP and reflected light of the EM grid. Middle: the corresponding low resolution EM overview of the area highlighted in the left image. Right: Overlay of the EM overview image with the corresponding Acs1-GFP signal from cryoLM. Scale bars: 1 μm. White star indicates were cryoET imaging was performed for panel (**B**).

(B) Acs1-GFP forms short ladder-like filament aggregates. Slices through the cryo-tomogram of the corresponding area indicated by white stars in (**A**). Note that short ladder-like filaments, visible in the magnified view (blue box), form an aggregate, which colocalizes with the Acs1-GFP fluorescent signal in (**A**). Single filaments are highlighted with blue arrowheads in the magnified view. Shown are projections of 9.15 nm thick slices. Scale bars: 100 nm.

(C) No filament bundles are visible in Acs1-GFP spreads. Spread meiotic yeast spheroplasts (6 h after induction of meiosis) for the indicated genotypes were analyzed by cryoEM as described in more detail in Figure S7B. Shown are percentages of spreads containing Acs1 filament bundles in EM images and the total number of spreads (n) analyzed for each genotype are indicated. Note that the experiment was performed together with the strains in Figure S7B. Therefore, the wilde-type *ACS1* strain was re-used in this figure.
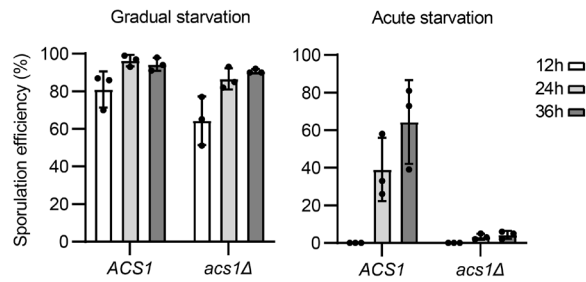
1164

1165 **Figure S11. Acs1 is needed for efficient sporulation after acute starvation.**

1166 Acs1 is needed for efficient sporulation after acute starvation. Yeast strains with the indicated genotypes
1167 were induced to enter meiosis by transfer from YPD to SPM (acute starvation), or by transfer from YPD
1168 to YPA to SPM (gradual starvation). The efficiency of ascospore formation was quantified by assessing
1169 the morphology of 100 cells from three independent experiments after 12, 24 and 36 h in SPM.
1170 Ascospore formation was considered successful if at least two spores were enclosed by a spore wall.
1171 Plotted values show the mean ± SD.
1172
1173
1174

1175 # SUPPLEMENTARY TABLES

1176 ## Table S1: cryoEM data statistical analysis

	Acs1 filament	Ald4 tetramer
Data collection and processing		
Nominal magnification	130,000	81,000
Voltage (kV)	300	
Electron exposure (e⁻/Å)	~60	
Defocus range (μm)	1.2 - 2.8	
Pixel size (Å/pixel)	1.07 (binning = 1)	1.10 (binning =1)
Symmetry imposed	C3 + helical (twist = 13.03˚, rise = 53.61 Å)	D2
Final particles (No.)	17,169	29,307
Map resolution (Å)	3.5	3.8
FSC threshold	0.143	
Refinement		
Map sharpening B factor (Å^2)	-83	-131
Model composition	(three layers)	
Atoms	48177 (Hydrogens: 135)	15416 (Hydrogens: 0)
Protein residues	6084	1980
Chains	18	4
Ligands with number	6R9: 9	NAP: 4
R.M.S deviations		
Bond length (Å)	0.022	0.019
Bond angles (˚)	1.73	1.769
Validation		
MolProbity score	1.50	1.27
Clashscore	7.19	5.14
Rotamer outlier (%)	0	0
Ramachandran plot		
Favored (%)	97.48	98.58
Allowed (%)	2.52	1.42
Outlier (%)	0	0
Masked CC	0.77	0.77

1177
1178

1179 **Table S2: Strain list**

Strain	Genotype*	Figure
YML9796 YML15193	*ndt80Δ::HIS3*	1A-D, 3A-E, S2, S3A-E, S4B-D,
YML9797 YML15194	*ndt80::HIS3 ZIP1::GFP(700)-HphMX4*	1A-D, 4A-B, 4D, 5B-D, S1B, S5B-C, S6A-E, S7A, S7C-D, S8A-D
YML12473	*ATP1-GFP::HIS3 ndt80Δ::HIS3*	1A-C
YML15200	*ald4Δ::ALD4^{WT}::LEU2::NATMX4*	3F
YML15201	*ald4Δ::ald4^{int}::LEU2::NATMX4*	3F
YML14301	***MATalpha ald4Δ::NATMX4*	3G
YML14249	** *MATa ALD4-yeGFP::KITRP1*	3G
YML14486	** *MATa ald4Δ::ALD4^{WT}-yeGFP::LEU2::TRP1::NATMX4*	3G
YML14717	** *MATalpha ald4Δ::ald4^{int}-GFP::LEU2::TRP1::NATMX4*	3G
YML10828	*ZIP1-GFP(700)::HphMX4*	4C-D, 5B-D, S6A-E, S7A, S7C-D, S8A-D
YML10774 YML12475 YML12476 YML12477	*'Wild-type'*	5F, 6C-D, S2, S4E, S5B, S7B, S9C, S11
YML12505 YML15195 YML15196	*acs1Δ::KanMX*	5F, 6D-E, 6G, S7B, S11
YML14830 YML15203	*acs1Δ::ACS1^{WT}::KITRP1::URA3::KanMX*	5E-F, 6E
YML14832 YML15202	*acs1Δ::acs1^{R264W}::KITRP1::URA3::KanMX*	5E-F, 6E
YML14833 YML15204	*acs1Δ::acs1^{K675A}::KITRP1::URA3::KanMX*	5E-F, 6E
YML12463 YML12507	*acs1Δ::ACS1^{WT}-GFP::TRP1::URA3::KanMX*	5G, 6C, S10C
YML12511	*acs1Δ::acs1^{K675A}-GFP::TRP1::URA3::KanMX*	5G
YML12471 YML12509	*acs1Δ::acs1^{R264W}-GFP::TRP1::URA3::KanMX*	5G
YML5909	*'Wild-type'*	6A-B
YML15066	*acs1Δ::ACS1^{WT}::KITRP1*	6G
YML15067	*acs1Δ::acs1^{R264W}::KITRP1*	6G
YML15069	*acs1Δ::acs1^{K675A}::KITRP1*	6G
YML4069	** *MATa*	7A
YML15199	** *MATalpha acs1Δ::KanMX*	7B
YML14653	** *MATalpha acs1Δ::ACS1^{WT}::KITRP1::URA3::KanMX*	7B
YML14612	** *MATalpha acs1Δ::acs1^{K675A}::KITRP1::URA3::KanMX*	7B
YML14510	** *MATalpha acs1Δ::acs1^{R264W}::KITRP1::URA3::KanMX*	7B
YML15198	*ald4Δ::KANMX4*	S4E
YML5095	*zip1Δ::KANMX4 ndt80Δ::HIS3*	S5A, S7B
YML15197	*ACS1-yeGFP::KITRP1*	S9, S10A-B

1180   * Unless indicated, all strains are diploid SK1 derivatives (*MATa/ MATalpha ho::LYS2 ura3 leu2::hisG*
1181   *trp1::hisG his3::hisG or ho::hisG leu2 ura3*) and homozygous for the genotype depicted in the table.

1182   ** haploid SK1 derivates (*MATa **or** MATalpha ho::LYS2 ura3 leu2::hisG trp1::hisG his3::hisG or*
1183   *ho::hisG leu2 ura3)*
1184

1185   **Table S3: Protein candidates for mitochondrial filaments**

1186   See separate Excel file

1187

REFERENCES

1. Lennon, J.T., and Jones, S.E. (2011). Microbial seed banks: the ecological and evolutionary implications of dormancy. Nat Rev Microbiol *9*, 119-130. 10.1038/nrmicro2504.

2. Rittershaus, E.S., Baek, S.H., and Sassetti, C.M. (2013). The normalcy of dormancy: common themes in microbial quiescence. Cell Host Microbe *13*, 643-651. 10.1016/j.chom.2013.05.012.

3. Aughey, G.N., and Liu, J.L. (2015). Metabolic regulation via enzyme filamentation. Crit Rev Biochem Mol Biol *51*, 282-293. 10.3109/10409238.2016.1172555.

4. Garcia-Seisdedos, H., Empereur-Mot, C., Elad, N., and Levy, E.D. (2017). Proteins evolve on the edge of supramolecular self-assembly. Nature *548*, 244-247. 10.1038/nature23320.

5. Hvorecny, K.L., and Kollman, J.M. (2023). Greater than the sum of parts: Mechanisms of metabolic regulation by enzyme filaments. Curr Opin Struct Biol *79*, 102530. 10.1016/j.sbi.2023.102530.

6. Lynch, E.M., Kollman, J.M., and Webb, B.A. (2020). Filament formation by metabolic enzymes-A new twist on regulation. Curr Opin Cell Biol *66*, 28-33. 10.1016/j.ceb.2020.04.006.

7. O'Connell, J.D., Zhao, A., Ellington, A.D., and Marcotte, E.M. (2012). Dynamic reorganization of metabolic enzymes into intracellular bodies. Annu Rev Cell Dev Biol *28*, 89-111. 10.1146/annurev-cellbio-101011-155841.

8. Park, C.K., and Horton, N.C. (2019). Structures, functions, and mechanisms of filament forming enzymes: a renaissance of enzyme filamentation. Biophysical Reviews *11*, 927-994. 10.1007/s12551-019-00602-6.

9. Simonet, J.C., Burrell, A.L., Kollman, J.M., and Peterson, J.R. (2020). Freedom of assembly: metabolic enzymes come together. Mol Biol Cell *31*, 1201-1205. 10.1091/mbc.E18-10-0675.

10. Noree, C., Begovich, K., Samilo, D., Broyer, R., Monfort, E., and Wilhelm, J.E. (2019). A quantitative screen for metabolic enzyme structures reveals patterns of assembly across the yeast metabolic network. Molecular Biology of the Cell *30*, 2721-2736. 10.1091/mbc.E19-04-0224.

11. Narayanaswamy, R., Levy, M., Tsechansky, M., Stovall, G.M., O'Connell, J.D., Mirrielees, J., Ellington, A.D., and Marcotte, E.M. (2009). Widespread reorganization of metabolic enzymes into reversible assemblies upon nutrient starvation. Proc Natl Acad Sci U S A *106*, 10147-10152. 10.1073/pnas.0812771106.

12. Noree, C., Sato, B.K., Broyer, R.M., and Wilhelm, J.E. (2010). Identification of novel filament-forming proteins in Saccharomyces cerevisiae and Drosophila melanogaster. J Cell Biol *190*, 541-551. 10.1083/jcb.201003001.

13. Shen, Q.J., Kassim, H., Huang, Y., Li, H., Zhang, J., Li, G., Wang, P.Y., Yan, J., Ye, F., and Liu, J.L. (2016). Filamentation of Metabolic Enzymes in Saccharomyces cerevisiae. J Genet Genomics *43*, 393-404. 10.1016/j.jgg.2016.03.008.

14. Noree, C., Monfort, E., Shiau, A.K., and Wilhelm, J.E. (2014). Common regulatory control of CTP synthase enzyme activity and filament formation. Mol Biol Cell *25*, 2282-2290. 10.1091/mbc.E14-04-0912.

15. Hansen, J.M., Horowitz, A., Lynch, E.M., Farrell, D.P., Quispe, J., DiMaio, F., and Kollman, J.M. (2021). Cryo-EM structures of CTP synthase filaments reveal mechanism of pH-sensitive assembly during budding yeast starvation. Elife *10*. 10.7554/eLife.73368.

16. Petrovska, I., Nüske, E., Munder, M.C., Kulasegaran, G., Malinovska, L., Kroschwald, S., Richter, D., Fahmy, K., Gibson, K., Verbavatz, J.M., and Alberti, S. (2014). Filament formation by metabolic enzymes is a specific adaptation to an advanced state of cellular starvation. Elife *3*. 10.7554/eLife.02409.

1233 17. Nüske, E., Marini, G., Richter, D., Leng, W., Bogdanova, A., Franzmann, T.M., Pigino, G., and
1234 Alberti, S. (2020). Filament formation by the translation factor eIF2B regulates protein synthesis
1235 in starved cells. Biol Open *9*. 10.1242/bio.046391.

1236 18. Stoddard, P.R., Lynch, E.M., Farrell, D.P., Dosey, A.M., DiMaio, F., Williams, T.A., Kollman,
1237 J.M., Murray, A.W., and Garner, E.C. (2020). Polymerization in the actin ATPase clan regulates
1238 hexokinase activity in yeast. Science *367*, 1039-1042. 10.1126/science.aay5359.

1239 19. Neiman, A.M. (2011). Sporulation in the budding yeast Saccharomyces cerevisiae. Genetics
1240 *189*, 737-765. 10.1534/genetics.111.127126.

1241 20. Marston, A.L., and Amon, A. (2004). Meiosis: cell-cycle controls shuffle and deal. Nat Rev
1242 Mol Cell Biol *5*, 983-997. 10.1038/nrm1526.

1243 21. Beck, M., and Baumeister, W. (2016). Cryo-Electron Tomography: Can it Reveal the Molecular
1244 Sociology of Cells in Atomic Detail? Trends Cell Biol *26*, 825-837. 10.1016/j.tcb.2016.08.006.

1245 22. Young, L.N., and Villa, E. (2023). Bringing Structure to Cell Biology with Cryo-Electron
1246 Tomography. Annual Review of Biophysics *52*, 573-595. 10.1146/annurev-biophys-111622-
1247 091327.

1248 23. Oelschlaegel, T., Schwickart, M., Matos, J., Bogdanova, A., Camasses, A., Havlis, J.,
1249 Shevchenko, A., and Zachariae, W. (2005). The yeast APC/C subunit Mnd2 prevents premature
1250 sister chromatid separation triggered by the meiosis-specific APC/C-Ama1. Cell *120*, 773-788.
1251 10.1016/j.cell.2005.01.032.

1252 24. Petronczki, M., Matos, J., Mori, S., Gregan, J., Bogdanova, A., Schwickart, M., Mechtler, K.,
1253 Shirahige, K., Zachariae, W., and Nasmyth, K. (2006). Monopolar attachment of sister
1254 kinetochores at meiosis I requires casein kinase 1. Cell *126*, 1049-1064.
1255 10.1016/j.cell.2006.07.029.

1256 25. Zachs, T., Schertel, A., Medeiros, J., Weiss, G.L., Hugener, J., Matos, J., and Pilhofer, M.
1257 (2020). Fully automated, sequential focused ion beam milling for cryo-electron tomography.
1258 Elife *9*, e52286. 10.7554/eLife.52286.

1259 26. Xu, L., Ajimura, M., Padmore, R., Klein, C., and Kleckner, N. (1995). NDT80, a meiosis-
1260 specific gene required for exit from pachytene in Saccharomyces cerevisiae. Mol Cell Biol *15*,
1261 6572-6581. 10.1128/mcb.15.12.6572.

1262 27. Loidl, J., Klein, F., and Engebrecht, J. (1997). Chapter 12 Genetic and Morphological
1263 Approaches for the Analysis of Meiotic Chromosomes in Yeast. In Methods in Cell Biology,
1264 M. Berrios, ed. (Academic Press), pp. 257-285. https://doi.org/10.1016/S0091-679X(08)60882-
1265 1.

1266 28. Loidl, J., Nairz, K., and Klein, F. (1991). Meiotic chromosome synapsis in a haploid yeast.
1267 Chromosoma *100*, 221-228. 10.1007/bf00344155.

1268 29. Jumper, J., Evans, R., Pritzel, A., Green, T., Figurnov, M., Ronneberger, O., Tunyasuvunakool,
1269 K., Bates, R., Žídek, A., Potapenko, A., et al. (2021). Highly accurate protein structure
1270 prediction with AlphaFold. Nature *596*, 583-589. 10.1038/s41586-021-03819-2.

1271 30. Varadi, M., Anyango, S., Deshpande, M., Nair, S., Natassia, C., Yordanova, G., Yuan, D., Stroe,
1272 O., Wood, G., Laydon, A., et al. (2022). AlphaFold Protein Structure Database: massively
1273 expanding the structural coverage of protein-sequence space with high-accuracy models.
1274 Nucleic Acids Research *50*, D439-D444. 10.1093/nar/gkab1061.

1275 31. Wettstein, R., Hugener, J., Gillet, L., Hernández-Armenta, Y., Henggeler, A., Xu, J., Van
1276 Gerwen, J., Wollweber, F., Arter, M., Aebersold, R., Beltrao, P., Pilhofer, M., and Matos, J.
1277 (unpublished). Waves of regulated protein expression and phosphorylation functionally rewire
1278 the proteome to drive gametogenesis.

1279 32. Morgenstern, M., Stiller, S.B., Lübbert, P., Peikert, C.D., Dannenmaier, S., Drepper, F., Weill,
1280 U., Höß, P., Feuerstein, R., Gebert, M., et al. (2017). Definition of a High-Confidence

1281   Mitochondrial Proteome at Quantitative Scale. Cell Rep *19*, 2836-2852.
1282   10.1016/j.celrep.2017.06.014.

1283   33.   Perez-Miller, S.J., and Hurley, T.D. (2003). Coenzyme Isomerization Is Integral to Catalysis in
1284   Aldehyde Dehydrogenase. Biochemistry *42*, 7100-7109. 10.1021/bi034182w.

1285   34.   Misonou, Y., Kikuchi, M., Sato, H., Inai, T., Kuroiwa, T., Tanaka, K., and Miyakawa, I. (2014).
1286   Aldehyde dehydrogenase, Ald4p, is a major component of mitochondrial fluorescent inclusion
1287   bodies in the yeast Saccharomyces cerevisiae. Biol Open *3*, 387-396. 10.1242/bio.20147138.

1288   35.   Holm, L. (2022). Dali server: structural unification of protein families. Nucleic Acids Research
1289   *50*, W210-W215. 10.1093/nar/gkac387.

1290   36.   Jogl, G., and Tong, L. (2004). Crystal Structure of Yeast Acetyl-Coenzyme A Synthetase in
1291   Complex with AMP. Biochemistry *43*, 1425-1431. 10.1021/bi035911a.

1292   37.   Ma, O.X., Chong, W.G., Lee, J.K.E., Cai, S., Siebert, C.A., Howe, A., Zhang, P., Shi, J., Surana,
1293   U., and Gan, L. (2022). Cryo-ET detects bundled triple helices but not ladders in meiotic
1294   budding yeast. PLoS One *17*, e0266035. 10.1371/journal.pone.0266035.

1295   38.   Takagi, T., Osumi, M., and Shinohara, A. (2021). Ultrastructural analysis in yeast reveals a
1296   meiosis-specific actin-containing nuclear bundle. Commun Biol *4*, 1009. 10.1038/s42003-021-
1297   02545-9.

1298   39.   Starai, V.J., and Escalante-Semerena, J.C. (2004). Acetyl-coenzyme A synthetase (AMP
1299   forming). Cellular and Molecular Life Sciences CMLS *61*, 2020-2030. 10.1007/s00018-004-
1300   3448-x.

1301   40.   Gulick, A.M., Starai, V.J., Horswill, A.R., Homick, K.M., and Escalante-Semerena, J.C. (2003).
1302   The 1.75 Å Crystal Structure of Acetyl-CoA Synthetase Bound to Adenosine-5'-
1303   propylphosphate and Coenzyme A. Biochemistry *42*, 2866-2873. 10.1021/bi0271603.

1304   41.   Starai, V.J., Celic, I., Cole, R.N., Boeke, J.D., and Escalante-Semerena, J.C. (2002). Sir2-
1305   dependent activation of acetyl-CoA synthetase by deacetylation of active lysine. Science *298*,
1306   2390-2392. 10.1126/science.1077650.

1307   42.   Van den Berg, M.A., and Steensma, H.Y. (1995). ACS2, a Saccharomyces cerevisiae gene
1308   encoding acetyl-coenzyme A synthetase, essential for growth on glucose. Eur J Biochem *231*,
1309   704-713. 10.1111/j.1432-1033.1995.tb20751.x.

1310   43.   Takahashi, H., McCaffery, J.M., Irizarry, R.A., and Boeke, J.D. (2006). Nucleocytosolic Acetyl-
1311   Coenzyme A Synthetase Is Required for Histone Acetylation and Global Transcription.
1312   Molecular Cell *23*, 207-217. https://doi.org/10.1016/j.molcel.2006.05.040.

1313   44.   Mews, P., Donahue, G., Drake, A.M., Luczak, V., Abel, T., and Berger, S.L. (2017). Acetyl-
1314   CoA synthetase regulates histone acetylation and hippocampal memory. Nature *546*, 381-386.
1315   10.1038/nature22405.

1316   45.   Vasiliou, V., Pappa, A., and Petersen, D.R. (2000). Role of aldehyde dehydrogenases in
1317   endogenous and xenobiotic metabolism. Chemico-Biological Interactions *129*, 1-19.
1318   https://doi.org/10.1016/S0009-2797(00)00211-8.

1319   46.   Schug, Z.T., Peck, B., Jones, D.T., Zhang, Q., Grosskurth, S., Alam, I.S., Goodwin, L.M.,
1320   Smethurst, E., Mason, S., Blyth, K., et al. (2015). Acetyl-CoA synthetase 2 promotes acetate
1321   utilization and maintains cancer cell growth under metabolic stress. Cancer Cell *27*, 57-71.
1322   10.1016/j.ccell.2014.12.002.

1323   47.   Shortall, K., Djeghader, A., Magner, E., and Soulimane, T. (2021). Insights into Aldehyde
1324   Dehydrogenase Enzymes: A Structural Perspective. Frontiers in Molecular Biosciences *8*.
1325   10.3389/fmolb.2021.659550.

1326 48. Kratzer, S., and Schuller, H.J. (1997). Transcriptional control of the yeast acetyl-CoA synthetase
1327   gene, ACS1, by the positive regulators CAT8 and ADR1 and the pleiotropic repressor UME6.
1328   Molecular microbiology *26*, 631-641. 10.1046/j.1365-2958.1997.5611937.x.

1329 49. Jacobson, M.K., and Bernofsky, C. (1974). Mitochondrial acetaldehyde dehydrogenase from
1330   Saccharomyces cerevisiae. Biochimica et biophysica acta *350*, 277-291. 10.1016/0005-
1331   2744(74)90502-6.

1332 50. Munder, M.C., Midtvedt, D., Franzmann, T., Nüske, E., Otto, O., Herbig, M., Ulbricht, E.,
1333   Müller, P., Taubenberger, A., Maharana, S., et al. (2016). A pH-driven transition of the
1334   cytoplasm from a fluid- to a solid-like state promotes entry into dormancy. Elife *5*, e09347.
1335   10.7554/eLife.09347.

1336 51. Joyner, R.P., Tang, J.H., Helenius, J., Dultz, E., Brune, C., Holt, L.J., Huet, S., Müller, D.J., and
1337   Weis, K. (2016). A glucose-starvation response regulates the diffusion of macromolecules. Elife
1338   *5*, e09376. 10.7554/eLife.09376.

1339 52. Walther, T., Létisse, F., Peyriga, L., Alkim, C., Liu, Y., Lardenois, A., Martin-Yken, H., Portais,
1340   J.C., Primig, M., and François, J. (2014). Developmental stage dependent metabolic regulation
1341   during meiotic differentiation in budding yeast. BMC Biol *12*, 60. 10.1186/s12915-014-0060-
1342   x.

1343 53. Ray, D., and Ye, P. (2013). Characterization of the metabolic requirements in yeast meiosis.
1344   PloS one *8*, e63707. 10.1371/journal.pone.0063707.

1345 54. Shvedunova, M., and Akhtar, A. (2022). Modulation of cellular processes by histone and non-
1346   histone protein acetylation. Nature Reviews Molecular Cell Biology *23*, 329-349.
1347   10.1038/s41580-021-00441-y.

1348 55. Wang, F., Zhang, R., Feng, W., Tsuchiya, D., Ballew, O., Li, J., Denic, V., and Lacefield, S.
1349   (2020). Autophagy of an Amyloid-like Translational Repressor Regulates Meiotic Exit. Dev
1350   Cell *52*, 141-151 e145. 10.1016/j.devcel.2019.12.017.

1351 56. O'Reilly, F.J., Xue, L., Graziadei, A., Sinn, L., Lenz, S., Tegunov, D., Blötz, C., Singh, N.,
1352   Hagen, W.J.H., Cramer, P., et al. (2020). In-cell architecture of an actively transcribing-
1353   translating expressome. Science *369*, 554-557. 10.1126/science.abb3758.

1354 57. Xue, L., Lenz, S., Zimmermann-Kogadeeva, M., Tegunov, D., Cramer, P., Bork, P., Rappsilber,
1355   J., and Mahamid, J. (2022). Visualizing translation dynamics at atomic detail inside a bacterial
1356   cell. Nature *610*, 205-211. 10.1038/s41586-022-05255-2.

1357 58. Hoffmann, P.C., Kreysing, J.P., Khusainov, I., Tuijtel, M.W., Welsch, S., and Beck, M. (2022).
1358   Structures of the eukaryotic ribosome and its translational states in situ. Nature Communications
1359   *13*, 7435. 10.1038/s41467-022-34997-w.

1360 59. Xing, H., Taniguchi, R., Khusainov, I., Kreysing, J.P., Welsch, S., Turoňová, B., and Beck, M.
1361   (2023). Translation dynamics in human cells visualized at high resolution reveal cancer drug
1362   action. Science *381*, 70-75. 10.1126/science.adh1411.

1363 60. Ho, C.M., Li, X., Lai, M., Terwilliger, T.C., Beck, J.R., Wohlschlegel, J., Goldberg, D.E.,
1364   Fitzpatrick, A.W.P., and Zhou, Z.H. (2020). Bottom-up structural proteomics: cryoEM of
1365   protein complexes enriched from the cellular milieu. Nat Methods *17*, 79-85. 10.1038/s41592-
1366   019-0637-y.

1367 61. Skalidis, I., Kyrilis, F.L., Tüting, C., Hamdi, F., Chojnowski, G., and Kastritis, P.L. (2022).
1368   Cryo-EM and artificial intelligence visualize endogenous protein community members.
1369   Structure *30*, 575-589.e576. 10.1016/j.str.2022.01.001.

1370 62. Tüting, C., Kyrilis, F.L., Müller, J., Sorokina, M., Skalidis, I., Hamdi, F., Sadian, Y., and
1371   Kastritis, P.L. (2021). Cryo-EM snapshots of a native lysate provide structural insights into a
1372   metabolon-embedded transacetylase reaction. Nat Commun *12*, 6933. 10.1038/s41467-021-
1373   27287-4.

63. Matos, J., Lipp, J.J., Bogdanova, A., Guillot, S., Okaz, E., Junqueira, M., Shevchenko, A., and Zachariae, W. (2008). Dbf4-dependent CDC7 kinase links DNA replication to the segregation of homologous chromosomes in meiosis I. Cell *135*, 662-678. S0092-8674(08)01363-9 [pii]

10.1016/j.cell.2008.10.026.

64. Scherthan, H., Wang, H., Adelfalk, C., White, E.J., Cowan, C., Cande, W.Z., and Kaback, D.B. (2007). Chromosome mobility during meiotic prophase in Saccharomyces cerevisiae. Proc Natl Acad Sci U S A *104*, 16934-16939. 10.1073/pnas.0704860104.

65. Giaever, G., Chu, A.M., Ni, L., Connelly, C., Riles, L., Véronneau, S., Dow, S., Lucau-Danila, A., Anderson, K., André, B., et al. (2002). Functional profiling of the Saccharomyces cerevisiae genome. Nature *418*, 387-391. 10.1038/nature00935.

66. Knop, M., Siegers, K., Pereira, G., Zachariae, W., Winsor, B., Nasmyth, K., and Schiebel, E. (1999). Epitope tagging of yeast genes using a PCR-based strategy: more tags and improved practical routines. Yeast *15*, 963-972. 10.1002/(sici)1097-0061(199907)15:10b<963::Aid-yea399>3.0.Co;2-w.

67. Schindelin, J., Arganda-Carreras, I., Frise, E., Kaynig, V., Longair, M., Pietzsch, T., Preibisch, S., Rueden, C., Saalfeld, S., Schmid, B., et al. (2012). Fiji: an open-source platform for biological-image analysis. Nat Methods *9*, 676-682. 10.1038/nmeth.2019.

68. Wild, P., Susperregui, A., Piazza, I., Dörig, C., Oke, A., Arter, M., Yamaguchi, M., Hilditch, A.T., Vuina, K., Chan, K.C., et al. (2019). Network Rewiring of Homologous Recombination Enzymes during Mitotic Proliferation and Meiosis. Mol Cell *75*, 859-874.e854. 10.1016/j.molcel.2019.06.022.

69. Salah, S.-M., and Nasmyth, K. (2000). Destruction of the securin Pds1p occurs at the onset of anaphase during both meiotic divisions in yeast. Chromosoma *109*, 27-34. 10.1007/s004120050409.

70. Matos, J., Blanco, Miguel G., Maslen, S., Skehel, J.M., and West, Stephen C. (2011). Regulatory Control of the Resolution of DNA Recombination Intermediates during Meiosis and Mitosis. Cell *147*, 158-172. https://doi.org/10.1016/j.cell.2011.08.032.

71. Faelber, K., Dietrich, L., Noel, J.K., Wollweber, F., Pfitzner, A.K., Mühleip, A., Sánchez, R., Kudryashev, M., Chiaruttini, N., Lilie, H., et al. (2019). Structure and assembly of the mitochondrial membrane remodelling GTPase Mgm1. Nature *571*, 429-433. 10.1038/s41586-019-1372-3.

72. Iancu, C.V., Tivol, W.F., Schooler, J.B., Dias, D.P., Henderson, G.P., Murphy, G.E., Wright, E.R., Li, Z., Yu, Z., Briegel, A., et al. (2006). Electron cryotomography sample preparation using the Vitrobot. Nat Protoc *1*, 2813-2819. 10.1038/nprot.2006.432.

73. Tivol, W.F., Briegel, A., and Jensen, G.J. (2008). An improved cryogen for plunge freezing. Microsc Microanal *14*, 375-379. 10.1017/S1431927608080781.

74. Schorb, M., and Briggs, J.A.G. (2014). Correlated cryo-fluorescence and cryo-electron microscopy with high spatial precision and improved sensitivity. Ultramicroscopy *143*, 24-32. https://doi.org/10.1016/j.ultramic.2013.10.015.

75. Mastronarde, D.N. (2005). Automated electron microscope tomography using robust prediction of specimen movements. J Struct Biol *152*, 36-51. 10.1016/j.jsb.2005.07.007.

76. Kremer, J.R., Mastronarde, D.N., and McIntosh, J.R. (1996). Computer visualization of three-dimensional image data using IMOD. J Struct Biol *116*, 71-76. 10.1006/jsbi.1996.0013.

77. Tegunov, D., and Cramer, P. (2019). Real-time cryo-electron microscopy data preprocessing with Warp. Nature Methods *16*, 1146-1152. 10.1038/s41592-019-0580-y.

78. Heebner, J.E., Purnell, C., Hylton, R.K., Marsh, M., Grillo, M.A., and Swulius, M.T. (2022). Deep Learning-Based Segmentation of Cryo-Electron Tomograms. J Vis Exp. 10.3791/64435.

79. Pettersen, E.F., Goddard, T.D., Huang, C.C., Meng, E.C., Couch, G.S., Croll, T.I., Morris, J.H., and Ferrin, T.E. (2021). UCSF ChimeraX: Structure visualization for researchers, educators, and developers. Protein Sci *30*, 70-82. 10.1002/pro.3943.

80. Castaño-Díez, D., Kudryashev, M., Arheit, M., and Stahlberg, H. (2012). Dynamo: a flexible, user-friendly development tool for subtomogram averaging of cryo-EM data in high-performance computing environments. J Struct Biol *178*, 139-151. 10.1016/j.jsb.2011.12.017.

81. Rosenthal, P.B., and Henderson, R. (2003). Optimal determination of particle orientation, absolute hand, and contrast loss in single-particle electron cryomicroscopy. J Mol Biol *333*, 721-745. 10.1016/j.jmb.2003.07.013.

82. Scheres, S.H.W. (2012). RELION: Implementation of a Bayesian approach to cryo-EM structure determination. Journal of Structural Biology *180*, 519-530. https://doi.org/10.1016/j.jsb.2012.09.006.

83. Zheng, S.Q., Palovcak, E., Armache, J.-P., Verba, K.A., Cheng, Y., and Agard, D.A. (2017). MotionCor2: anisotropic correction of beam-induced motion for improved cryo-electron microscopy. Nature Methods *14*, 331-332. 10.1038/nmeth.4193.

84. Zhang, K. (2016). Gctf: Real-time CTF determination and correction. J Struct Biol *193*, 1-12. 10.1016/j.jsb.2015.11.003.

85. Zivanov, J., Nakane, T., Forsberg, B.O., Kimanius, D., Hagen, W.J.H., Lindahl, E., and Scheres, S.H.W. (2018). New tools for automated high-resolution cryo-EM structure determination in RELION-3. Elife *7*, e42166. 10.7554/eLife.42166.

86. He, S., and Scheres, S.H.W. (2017). Helical reconstruction in RELION. Journal of Structural Biology *198*, 163-176. https://doi.org/10.1016/j.jsb.2017.02.003.

87. Sanchez-Garcia, R., Gomez-Blanco, J., Cuervo, A., Carazo, J.M., Sorzano, C.O.S., and Vargas, J. (2021). DeepEMhancer: a deep learning solution for cryo-EM volume post-processing. Communications Biology *4*, 874. 10.1038/s42003-021-02399-1.

88. Emsley, P., Lohkamp, B., Scott, W.G., and Cowtan, K. (2010). Features and development of Coot. Acta Crystallogr D Biol Crystallogr *66*, 486-501. 10.1107/s0907444910007493.

89. Song, Y., DiMaio, F., Wang, R.Y., Kim, D., Miles, C., Brunette, T., Thompson, J., and Baker, D. (2013). High-resolution comparative modeling with RosettaCM. Structure *21*, 1735-1742. 10.1016/j.str.2013.08.005.

90. Adams, P.D., Afonine, P.V., Bunkóczi, G., Chen, V.B., Davis, I.W., Echols, N., Headd, J.J., Hung, L.W., Kapral, G.J., Grosse-Kunstleve, R.W., et al. (2010). PHENIX: a comprehensive Python-based system for macromolecular structure solution. Acta Crystallogr D Biol Crystallogr *66*, 213-221. 10.1107/s0907444909052925.

91. Krissinel, E., and Henrick, K. (2007). Inference of macromolecular assemblies from crystalline state. J Mol Biol *372*, 774-797. 10.1016/j.jmb.2007.05.022.

92. Gouet, P., Courcelle, E., Stuart, D.I., and Métoz, F. (1999). ESPript: analysis of multiple sequence alignments in PostScript. Bioinformatics *15*, 305-308. 10.1093/bioinformatics/15.4.305.